UNIVERSITY OF CAPE TOWN

Faculty of Engineering and the Built Environment

Department of Mechanical Engineering

Growth in a Computational Planning Pipeline for Treatment in Patient-Specific Coarctation of the Aorta.

MSc Student: Nasonkwe Hampwaye
Student ID: HMPNAS001
Supervisor: Associate Prof. Malebogo Ngoepe
In Collaboration with: Jie Wang (at the University of Manchester)

A dissertation submitted in fulfilment of the requirements for the degree:

MSc in Mechanical Engineering

Submission date: 11th February 2024.

Plagiarism Declaration

I know the meaning of plagiarism and declare that all the work in the document, save for that which is properly acknowledged and referenced, is my own. This thesis/dissertation has been submitted to the Turnitin module (or equivalent similarity and originality checking software) and I confirm that my supervisor has seen my report and any concerns revealed by such have been resolved with my supervisor.

Signed by candidate

Signature:

Abstract:

Coarctation of the Aorta (CoA) is a Congenital Heart Disease (CHD) that is present at birth and is usually detected in the early years of the child. In the individualized treatment of a CoA patient, a non-severe case which initially exhibits no symptoms, and thus no treatment is necessary, could potentially turn severe due to the growth of the baby. Growth is characteristic of living structures including the aorta and is understood to occur in response to a given mechanical environment.

In the African context, limitations to adequate planning of treatment exist. This includes the geographic and economic situations that limit the patients from accessing full and follow-up treatment. Herein lies the importance of this study. The creation of the Partnerships in Congenital Heart Disease in Africa (PROTEA) project has opened the opportunity to investigate causative genes and molecules of CHD with a focus on CoA in Southern Africa.

This particular study has been structured to tackle the model-based patient specific long-term prediction of growth which could potentially assist in clinical assessment of CHD. To this end, a computational model for aortic growth, through a manually coupled framework was developed. The collaborative work carried out by *Jie Wang*[1] included Computational Fluid Dynamics (CFD) modelling of the haemodynamics in the patient-specific aorta. The mechanical stresses of circumferential pressure (σ_θ) and wall shear stress (WSS), that drive growth, were of particular interest in this study to model growth. An Agent Based Model (ABM) that encompassed the complex mechano-chemo-biological process of aortic growth was chosen and employed in alignment with the PROTEA project aforementioned goals. The ABM agents that played a key role in growth were identified as the Endothelial cells (EC) and Smooth Muscle Cells (SMC). The interaction rules of these agents, that were induced by the WSS and σ_θ obtained from the CFD, were specified by mathematical representations of the concentration gradient of growth factors and growth hormones; PDGF-AB, TGF-β and NO, directly affecting the SMC proliferation and apoptosis rates. The ABM ultimately predicted growth by translating the SMC proliferation to vascular wall thickness; and luminal radius and growth rate after employing further processing. A comparative medical study was leveraged to develop a species-specific ABM by considering the rat (abdominal aorta), porcine (carotid artery) and healthy toddler (abdominal aorta) species commonly used in cardiovascular research. This was done because of the lack of homogenized experimental research data for human toddlers required to create a comprehensive set of ABM rules. This exercise was carried out by modifying the aortic geometric parameter values and the input mechanical stresses to each species.

The ABM prediction accuracy with respect to the luminal radius was observed to be 79% in the rat, above 95% in porcine and 91.6% in the healthy toddler case. Alternatively, the ABM prediction accuracy with respect to the growth rate was 38.7% in the rat, 90% in porcine and 64.3% in the healthy toddler. However, a further literature search revealed a 100% accuracy for the healthy toddler case. Given its performance, the ABM was adapted to the patient specific case. Thus, growth was modelled in a 2.5-year-old patient-specific CoA. It was predicted that at age 3, the patient needed intervention as their coarctation would not resolve with age. In addition, the blood pressure and wall shear stress were studied after the predicted growth to further contribute to informing treatment/intervention planning. The patient is predicted to develop High Blood pressure by age 3 and turbulent flow patterns increase, thus increasing the chances of injury to the vessel and developing aneurysms or thrombosis.

[1] *Jie Wang* | PhD Student
Mechanical, Aerospace & Civil Engineering | School of Engineering
Faculty of Science and Engineering | The University of Manchester

To improve the prediction for intervention planning, the ABM should include the remodeling process to the growth process.

Keywords: agent-based model, growth model, species-specific agent-based model, coarctation, patient-specific aortic growth

Acknowledgements

This thesis is a testament to the immeasurable contributions of many that made this research process worthwhile.

Firstly, I would like to extend my sincere gratitude to Associate Professor Malebogo Ngoepe for her guidance, motivation, patience, financial assistance, and the host of opportunities she has presented to me throughout the course of my study. Her extensive knowledge in the field of biomechanics is inspiring at the very least. She also exhibited a kindness and faith that was far above obligation. I am truly indebted to her.

I owe a massive thankyou to Jie Wang, without whom this work would not be possible. Her CFD contribution upon which this research is intertwined has been vital to the success of this study. Her willingness to engage and work out ways to best harmonize our studies has been nothing short of selfless and we have built a friendship through this process.

Thank you to Professor Alistair Revell, from the University of Manchester for his immense input to my research. His experience, guidance, and readiness to assist in the research process has been invaluable.

I would like to thank Liam Swanson, upon whose fundamental work this research rests. His meticulous study and willingness to share his work has been key to this research being successful. In addition, I would like to thank the PROTEA team at Red Cross War Memorial Children's Hospital; Prof John Lawrenson and Dr Thomas Aldersley for assisting in gaining a deeper insight into the clinical and technical aspects of testing and treating CoA. My gratitude extends to Prof Liesl Zuhlke, Prof Bernard Keavney and Dr Emily Manchester.

Thank you to CERECAM. This research group has been vital in helping me look at my research from different points of view. The discussions during various academic exercises have contributed to gaining a more wholistic approach to my research.

Lastly, I would like to thank God for His many mercies and graces tangible through my family and friends. I will forever be grateful for the financial, mental, emotional, and spiritual; and sometimes academic needs that they have filled during my academic journey. To my dear father: Godfrey, mother: Cecilia, and siblings: Chikuba and Eba, I will be eternally grateful for your support, patience, understanding and love.

Table of Contents

Chapter 1: INTRODUCTION

1.1 Background

CHD is a condition present at birth in which the child presents with a malformation or missing altogether of parts of the heart structure. About 41% of the 11 000 babies estimated to be born with CHD per year need surgery. 25% of babies born with a heart defect have critical CHD, i.e. they need surgery within their first year of life [2]. However, 85% of these children are expected to survive to adulthood given that they have access to proper care [1].
One of these critical CHD conditions is CoA. The word "coarctation" is derived from the Latin verb "coartare," which means "to press together." As seen in Figure 1.1, coarctation of the aorta is characterised by a constriction or stenosis of the aorta, either in one region or along a portion of its length [3].
This condition forces the heart to pump blood through the CoA more forcefully than it would normally [4]. The ventricular muscles need to work harder to force blood out of the heart because of the constriction, which also causes blood to flow back into the left ventricle of the heart. The descending section of the aorta is where coarctation typically manifests, causing low blood pressure and weak pulses in the lower body and limbs, as well as normal or high blood pressure resulting in the arms and head. In cases of extreme CoA, blood would be less likely to flow to the lower body. This is likely to cause a weakened heart muscle as the heart muscle is thickened in response to the amount of force it is required to exert to sustain blood flow.

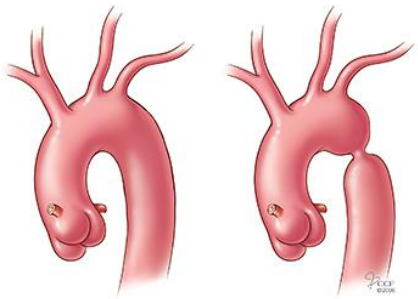

Figure 1.1: Normal aorta (Left) Vs Coarctation in aorta (Right) [3].

Signs and symptoms of severe CoA in babies may appear soon after birth. These consist of: [4]
1. Pale complexion
2. Sensitivity
3. Excessive perspiration
4. Having trouble breathing
5. Having trouble eating

If left untreated, CoA can lead to heart failure or death. Therefore, intervention within the few months after birth is required to dodge or alleviate the serious problems that are likely to develop. Diagnosis of CoA in babies depends on the severity of the signs and symptoms at that time. One test to determine the blood's oxygen saturation level is pulse oximetry. It is a simple, painless way to gauge how well oxygen is received by the body's farthest-reaching organs, like the arms and legs [5]. It is conducted during new born screening and is one of the ways used to detect heart defects during the first few days of life [2]. If suspected, a series of tests are ordered by the doctor to confirm the presence of CoA and also develop an appropriate treatment plan for the patient. Below is a summary of the tests:[4]

1. **Echocardiogram (Echo)**. Echo takes advantage of the nature of reflection of sound. A probe that emits sound waves is placed on the chest and moving images are developed on a screen based on the reflected sound waves. An echo is able to locate the CoA and ascertain its severity.
2. **Electrocardiogram (ECG)**. The electrocardiogram (ECG) records the electrical signals from the heart on paper or a computer monitor by placing electrodes on the wrists, ankles, and chest. Ventricular hypertrophy, which is linked to the severe case of CoA, can be detected by the ECG.
3. **Chest X-ray.** An inflated portion of the aorta, a constriction at the location of the coarctation, or both may be visible on a chest X-ray.
4. **Magnetic Resonance Imaging (MRI).** An even more comprehensive option to the Echo is the MRI. Radio waves and a strong magnetic field are used in place of sound waves. Similar to Echo, MRI can show where and how severe the CoA is, as well as whether it affects any other blood vessels in your body.
5. **Computerised tomography (CT) scan.** With a succession of X-rays, detailed cross-sectional images of your body are created. The arteries and veins are used to track blood flow by injecting a tracer into the bloodstream. It is possible to identify further cardiac abnormalities and ascertain the location and severity of the CoA as well as how it affects other blood arteries in your body.
6. Catheterization of the heart. Using X-ray imaging, a catheter is threaded to your heart through an artery or vein in the iliac region, arm or neck. To improve the heart's visibility on the X-ray images, a dye may be administered through the catheter. Additionally, the dye can be used to gauge the oxygen and pressure within the heart's chambers.

Once confirmed, the baby will go through either surgery to cut out the narrowed section and re-join the two free ends or have a less invasive procedure called balloon angioplasty. Angioplasty involves a catheter being inserted at the groin, into the heart through the blood vessels with a balloon on the end of it. The balloon is inflated once it arrives at the site of CoA so as to dilate the aorta fully. After which the catheter is withdrawn [3].

In alignment with the realization of the United Nations', 2016, Sustainable Development Goals, CHD has gradually gained traction as a vital contribution to reducing under-5 deaths [61]. Regretfully, there is a scarcity of accurate and contemporary epidemiological data from low-income and African nations [62]. Similarly, there is a gap in studies pertaining to mapping of the genome onto CHD related phenotypic traits and the associated contributions of the environment in the sub-Saharan population [63]. As the cradle of humankind, Africa comprises the most genetically varied society. Identification of genetic mutations/variants that cause CHD in this diverse population would be valuable [64].

The purpose of the PROTEA project was to determine if it would be viable to maintain a sizeable database containing both genetic and phenotypic data in Southern Africa. This would establish the foundation required for subsequent research to fill in the information vacuum in the area regarding CHD [62]. This project has two noteworthy goals: Aim 2 will look into the genetic and molecular causes of CHD in the area and Aim 3 will demonstrate how to use CFD to study CoA and eventually help with clinical evaluation of CHD [65], including long-term growth and remodelling prediction from local blood flow. Thus, allowing for patient-specific outcome assessment based on a model [62].

Taking advantage of PROTEA Aim 2, the modelling tool used in this study to achieve Aim 3 is the ABM which is discussed in detail in Chapter 2.3. ABM is a contemporary method for researching and modelling intricate mechano-chemo-biological reactions at the cellular level [22]. Growth hormones such as TGF-β and PDGF-AB are said to directly influence growth after being activated by mechanical stresses through the process of mechanotransduction [66]. Therefore, to be able to use a modelling tool that can incorporate the genetic markers considered in Aim 2 to determine growth and remodelling in Aim 3 would be a step towards harmonizing the aims.

1.2 Problem Identification

Even after surgery, children with a CoA often have hypertension that is treated with medicine [2]. They also are exposed to a heightened risk of aneurysm formation due to the healing process in the artery after the surgery, as well as the risk of recoarctation occurring. Therefore, Children and adults with CoA should see a cardiologist (a cardiac specialist) on a regular basis to keep track of their development and be checked for these and other potential health issues as they age [2]. The weight of poverty is particularly great in Africa. Knowing that the patient's location and financial circumstances prevent them from receiving the best treatment possible worsens the frustration for both families and medical staff [6]. With this in mind, it would be useful to track the growth and remodelling on the aorta and its effects. This information will help in the more efficient planning of intervention and post-intervention care of CoA patients. In addition, we can reduce the number of visits the patient needs to make to the cardiologist, thus reducing the burden on the health system and patients, by studying growth and remodelling and predicting potential problems and the time frame they are likely to occur using the growth model we will develop.

Living structures show the ability to grow and adapt their form, shape and microstructure to a given mechanical environment. Growth is characterised by intricate molecular-level mechano-chemo-biological reactions that control cell-mediated tissue adaptations [23]. Similarly, the aorta grows in order to sustain the patient's growing body. This study navigates through the process of considering growth at a multi-scale level and its effects on the patient's coarctation.

1.3 Aims and Objectives

Aims

The goal of this study is to computationally model the growth of a patient-specific CoA aorta using Agent Based Modelling in order to include the complex mechano-chemo-biological nature of growth.

Objectives

- Gain comprehension of the mechanisms involved in aortic growth in Agent Based Models.
- Select relevant ABM agents and rules to describe growth in the Aorta.
- Implement ABM agents to represent aortic anatomy and rules to represent the complex aortic growth in NetLogo and generate suitable results.
- Compute aortic growth from ABM results and observe its subsequent effects on haemodynamic patterns of the patient.
- Develop manual coupling mechanisms for the transfer of geometric and haemodynamic data between CFD and ABM.
- Develop an ABM to predict species-specific growth by using the comparative medicine approach.

1.4 Scope & Limitations

With biological model building, it is an important step to be able to validate the model against experimental data. Literature-derived values were used for validation. Human experimental data from literature was limited as well; therefore, a comparative medicine approach was used to arrive at a meaningful model. Three phases are considered. First, the rat aorta and porcine carotid artery growth models are developed, then a healthy human baby aorta growth model is built, and finally, the patient specific case is considered.

As already stated above the aim of this study is to be able to create the growth model to be used in the African environment. Although MRI would be the best suited image source, echocardiograms are in wide use in paediatric contexts and our approach seeks to interface with existing technology. This introduces some challenges to the image reconstruction process, where echocardiograms require more input and manipulation in order to obtain useful images for model development. In addition, haemodynamic flow parameters are time averaged. These parameters are necessary in obtaining mechanical stresses acting on the aorta walls that contribute heavily to growth. Growth is observed to result from sustained mechanical stresses below some threshold over a period of time, which supports the assumption to take an average of the haemodynamic flow parameters. However, above some threshold, the mechanical stresses are likely to cause damage to the vessel, thus leading to the change in the material properties of the vessel wall, i.e. remodelling. In this pathological case, the time averaged haemodynamic flow parameters are a limitation as it loses valuable information that more accurately reflects the vessel's growth [10].

1.5 Roadmap of Thesis

Growth is defined and explored in Chapter 2. With that understanding, the modelling tool used in this study, Agent Based Modelling (ABM) is introduced.

Chapter 3 first introduces the overall pipeline of model development used to mimic growth. A more detailed development of the ABM is then given. By comparative medicine, different cases are considered. First the rat aorta growth model is developed and compared against experimental data in literature for validation of the model. The effects of different mechanical stresses on the vessel wall (blood pressure and wall shear stress (WSS)) are then studied. In a similar way, the porcine carotid artery growth model is developed and validated. Phase 2 then builds the model for a healthy human baby and the model is validated by comparing to literature average values of human aorta dimensions during toddler years. Finally, we develop a patient specific growth model and predict growth in that particular case. The resulting haemodynamics after growth are then studied to predict the effects of growth on the aorta.

Chapter 4 goes on to present the results of the model, and a discussion of the results is carried out in Chapter 5. After which, the conclusion of the study is made in Chapter 6.

Chapter 2: LITERATURE REVIEW

2.1 Growth

Growth is one of the attributes that characterises living organisms from dead organisms or inanimate objects [7]. Growth in this case refers to the change in mass. The mass change can be observed in one of three ways;[8]

(i) mass addition at constant density, as observed in soft tissue development.
(ii) density change at constant volume, as observed in bone densification; and
(iii) both (i) and (ii) as observed in bone development.

Living structures show the ability to grow and adapt their form, shape and microstructure to a given mechanical environment [9]. The evolution of material properties due to the living structure's adaptation to microstructural changes without changes in mass is referred to as remodelling. Although growth and remodelling are different processes, growth can initiate remodelling, which determines the overall behaviour of tissue [8]. Morphogenesis, on the other hand, is the macroscopic change caused by growth and remodelling [9]. Growth and remodelling are crucial for homeostasis (regulation of a dynamic equilibrium within the healthy limits in a biological system) and early life processes including morphogenesis, as well as pathogenesis (development of disease) in adult tissue, which often adjusts to alterations in its chemo-mechanical surroundings brought on by ageing, disease, trauma, or surgical procedures [10].

Growth can also be looked at from the perspective of tip growth as seen in plant roots, surface or accretive growth e.g., in shells, and volumetric or bulk or interstitial growth as observed in muscles, solid tumours, the heart and arteries. Volumetric growth refers to processes in which local volume elements in the structure alter over time instead of just at the boundary [8]. It is crucial to note that an organism's growth is more complex than just a simple enlargement, at a specified scale factor, of its structure from birth. Growth in living organisms is said to be allometric i.e., relative growth of an organ to the total weight of the organism. Huxley's [11] mathematical representation of growth focuses on the mass, m, or length, l, of an organ scaled as a power of the organism's total mass, M.

$$m = kM^{\alpha} \tag{2.1.1}$$

here,

α = 1 shows isometric growth

α ≠ 1 shows allometric growth

If k and α are constant, that implies that an organism's and an organ's respective growth rates are proportionate.

$$m = kM\alpha \Rightarrow \frac{\dot{m}}{m} = \alpha\frac{\dot{M}}{m} \tag{2.1.2}$$

Furthermore, organs have the ability to adapt or maladapt by growth and/or remodelling in response to neurohormonal, chemical and mechanical cues. It follows that hypertrophy (increase in the volume of cells) is stimulated by both chemical cues (e.g., growth factors, hormones) and mechanical cues (e.g., stress and strain) [12]. Therefore, there are two sources of growth:[9]

1. Mechanically driven growth: where growth is triggered by stress or strain.
2. Biochemically/ Morphogenetic growth/ Morpho-elasticity: the tissue's form is changed by an underlying biological system. This modifies a system's mechanical behaviour and function.

Physical, geometric, and mechanical constraints on the development of a tissue or organ must be combined with genetic and biochemical cues to provide a complete picture of growth [8].

This brings about the question of what really drives growth and remodelling? Do the inherent genetics initiate growth and remodelling which will in turn drive the mechanics or do the mechanical stimuli

drive the biological responses of growth and remodelling by cells? Mechano-transduction is the process by which mechanical signals applied in the volume or at the boundary of a body are mediated down to cellular level and transferred to the nucleus [66].
From whichever angle that we approach growth and remodelling, both cases complement each other as they aim to comprehend issues related to growth and remodelling during an organism's life as well as structure-function connections [10].

Tissue growth is characterised by a change in tissue mass and structure and is caused by the synthesis of new proteins, cells, and other material particles at the microscopic level. The material supply toy-tissue model can be used to simulate growth in its most basic and realistic form. as illustrated in Figure 2.1 Comparing the Toy-tissue microscopic model, a-f, to the macroscopic

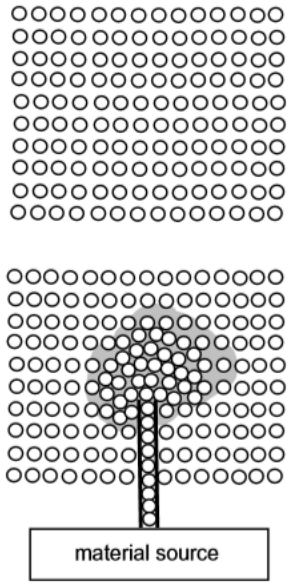

Figure 2.1: A microstructural toy-tissue model of material supply [13].

theory, A-F (compare the respective lower case and upper-case points) it is observed that:[13]

a) The quantity of balls in the system rises as more are supplied

b) a higher concentration of the balls is observed around the point of entry of the balls and these new balls do not disseminate uniformly

c) the new balls disseminate in the immediate region of the point of entry as they cannot be accommodated at the point of entry, thus the balls get denser in the region of injection

d) less room is left over for the new balls when more balls are supplied into the system

e) new balls press the old ones

f) new balls tend to expand the area occupied by the tissue when overall ball rearrangements

reach the tissue surface.

A) tissue mass increases.

B) mass density fluctuates at a certain location which implies that mass increase is not uniform.

C) diffusion of mass is observed.

D) diffusion depends on the mass density and the structure of the tissue at any particular time, as denser tissues can hold less material.

E) stresses develop as growth occurs.

F) tissue expands in proportion to volume.

This toy-tissue model is of particular interest to this study because its simplistic nature is able to capture growth at multi-scales by considering the effects of the balls, which could represent cells, on the system, which represents the tissue. The change in density would lead to a subsequent change in the material properties of the tissue. This model also captures inhomogeneous growth which is characteristic of growth observed in nature. Therefore, the toy-tissue model provides a good framework for growth at a low level (simplistic level).

2.2 Soft Tissue Growth

Tissues that surround, attach to, or support other human organs and structures are referred to as soft tissues. Muscles, tendons, ligaments, fascia, nerves, fibrous tissues, fat tissue, blood vessels, and synovial membranes are examples of soft tissue [14]. All living things exhibit mechanical behaviour that is influenced by both the viscoelastic response to loading on short time intervals, up to several minutes, and the growth and remodelling responses, which are often essential, on time scales ranging from hours to months [10].

Initially before we look at the smaller scale of the organism, we could think of modelling the growth of the whole organism using height. Quetelet [15], by obtaining and analysing the Belgian height data, suggested a model for change of height, H(t) over time, t, as

$$H(t) = at + \frac{b+t}{1+\frac{4}{3}t} \tag{2.2.1}$$

This was considered to be the first application of the Gaussian distribution in a statistical study. Furthermore, in his attempt to relate mass, M, to height, H(t), Quetelet [15] proposed the relation,

$$M = cH^{\alpha} \tag{2.2.2}$$

Here,

c is the body mass index

$\alpha = \frac{5}{2}$ in childhood

$\alpha = 2$ in adults

Note that this scaling law relation is independent of time. Putter [8] later on attempted to model the evolution of mass from physical principles. It is inherent to assume that for growth to occur, the rate of new material added should be higher than that which leaves the system. Typically, the rate of material removal is assumed to be proportional to the mass itself, M(t), as in the standard exponential decay problem. On the other hand, the rate of material addition is proportional to a power of the mass. Hence, we have [8]

$$\dot{M} = M(aM^{-p} - b) \tag{2.2.3}$$

$\dot{M} = \frac{dM}{dt}$ and ab > 0

By solving for M, for p=0, we obtain the simple exponential process

$$M(t) = M_0 e^{(a-b)t} \tag{2.2.4}$$

where M_0 is the mass at birth.

If however, we do solve for p ≠ 0 we have

$$\left(\frac{M(t))}{M_\infty}\right)^p = 1 - \left(1 - \left(\frac{M_0}{M_\infty}\right)^p e^{-bpt}\right) \tag{2.2.5}$$

where $M_\infty = \left(\frac{a}{b}\right)^{\frac{1}{p}}$ is the asymptotic mass.

As simplified and realistic as this mass-growth model is when we look at whole organisms, we will run into a problem if attempts are made to use this model for scaled down systems of the organism, i.e. organs, tissue and cells. It was expressed earlier in this paper that no adult organism is a pure dilation of itself at birth. This also applies to the case of organs and whole organisms, they do not grow at the same rate, either. Therefore, different approaches were developed to model organ and tissue growth.

Biochemical models for growth cannot predict changes in geometry, structure and mechanical properties during growth and remodelling in soft tissue. These three changes are important because they directly affect blood circulation in arteries. The following three mechanical models (Chapter 2.3.1 A., B., and C.) have been created to fully describe growth and remodelling at the tissue and organ level:[12]

2.3 Computational Models of Growth

For the purpose of conceptualising the intricate network of mechanobiological processes involved in arterial adaptation, computational models can be a useful tool [37][38]. In the field of computational modelling of vascular pathophysiology; equation-based models, and agent-based models (ABMs) are the two main modelling classes that are used. Continuous models that are based on systems of partial differential equations (PDEs) or ordinary differential equations (ODEs) are known as equation-based models. While PDEs capture the evolution of the system state variables in both space and time, ODEs are utilised to describe the temporal change of those variables [25]. Numerical techniques, such as the finite difference method, finite element method (FEM), or finite volume approach, are required to address PDE systems related to solid mechanics or fluid dynamics problems because of the intricate geometry of the vascular segments [26].

2.3.1 Equation-based Models

A. Structural Adaptation theory

Structural adaptation theory refers to the process by which a structure, i.e. tissue or organ becomes fitted to its environment. It involves the complexities of the tissue or organ, i.e., its constitutive parts, and how these individual parts morph and work in synchrony to optimize the mechanical work of the tissue or organ [12]. An example is Arts' [16] model consisting of adjoining cylindrical shells to model the remodelling of heart myofibre orientation (in addition to heart wall thickness) adapted in each shell to optimize local deviation of fibre shortening during systole (contraction of the heart ventricles) and sacomere lengthening, at the beginning of blood ejection from the heart ventricle, from their corresponding prescribed set points.

B. Volumetric Finite Growth theory

This theory looks at growth as a deformation. Since soft tissue does not necessarily experience isotropic growth, we require a tensor description for this growth. The growth tensor, G, at each point of the structure describes a change in the local volume element [8]. Hooke's law does not hold well for animal tissues, except bone [93]. However, they exhibit nonlinear pseudo-elastic responses to finite strains. For this reason, nonlinear continuum mechanics is best suited to study the mechanical behaviour of biological tissue. Since soft tissue behaves more like viscoelastic polymers than inanimate objects, finite elasticity is utilised to study biomechanics. Additionally, elastomers are increasingly being used in both scientific and clinical medicine [17]. In order to more accurately model growth specific to the physiological system being considered (in this paper, the aorta), we have to add the kinematic and kinetic equations of growth to the classical set of kinematic equations, kinetic equations and constitutive relations.

Consider the motion $\phi : B_0 \rightarrow B_f$ that maps an initial reference configuration, B_0, to a current configuration, B_f , via x(X,t) = ϕ (X,t) where, x(X,t) is the position of a volumetric material point at time, t, originally located at X at t = 0. The deformation gradient, F, can then be defined as

$$F = \nabla\varphi = \frac{\partial x}{\partial X} \tag{2.2.6}$$

Recent models are based on the idea that deformation can been split into the growth part, g, and the elastic part, e, in order to describe growth. Creating the multiplicative composition.

$$F = F^e . F^g \tag{2.2.7}$$

F^g describes the addition (or subtraction) of mass to a local volume element prescribed constitutively, either directly or in rate form to characterize the evolution of growth. This is to say that it is taken into consideration that a volume can be divided into infinitely small volume points, therefore, addition (or subtraction) to each point is tracked separately. If F^g is established it is possible to solve the equations either analytically, for simple geometries, or numerically, using non-linear finite element solvers [9]. F^g produces an incompatible growth configuration, ν , which lies between B_0 and B_f and does not describe the gradient of the vector field. This, simply put, means that the initial volume of the living system may no longer fit together, i.e., incompatible. The idea that these volumes must be deformed elastically, it follows that a growth-induced residual stress is required for the continuum to stay open and free of overlaps [10]. Therefore, as an object grows, we assume a virtual stage at which material is added to the object and then conclude with the elastic step that returns the object to its shape in the living organism, i.e. ensuring compatibility of the volume [18].

A summary of this theory has been illustrated in Figure 2.2. We can relate the volume elements to their material counterparts through,

$$J = det(F) = J_e.J_g \tag{2.2.8}$$

where J_e is reversible and J_g is irreversible and describes the volumetric growth.

In addition, if we let θ be used to describe an observable growth parameter then, we can

capture volumetric anisotropic growth as:[9] $\theta_1 n_1 \otimes n_1 + \theta_2 n_2 \otimes n_2 + \theta_3 n_3 \otimes n_3$

The density, ρ_0 , of the newly grown volume is not identical to the initial tissue volume, hence to account for these density changes independent of the growth tensor, open system thermodynamics are applied to the tissue system. The conservation of density requires the inclusion of new parameters to the mass balance, such as cell migration through mass flow, R, from an extra mass source, R_0 [19].

$$\rho_0 = \rho_0^* + \int_0^t \nabla (R) + R_0 \, d\tau \tag{2.2.9}$$

here, ρ_0^* - initial density prior to growth

ρ_0 - density of tissue after apposition of new mass

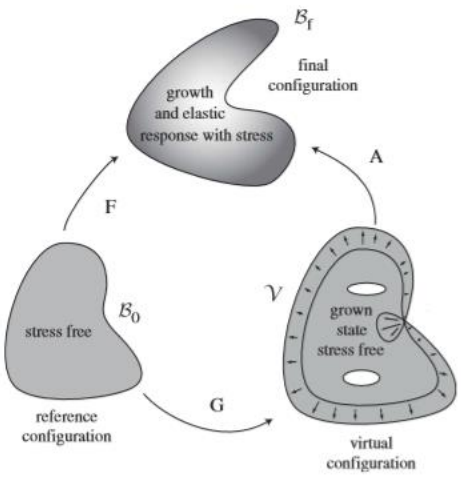

Figure 2.2: The breakdown of finite growth. The reference configuration B_0 (is mapped onto the present configuration B_f by the deformation gradient F. The product of an elastic deformation tensor A and a growth tensor G can be used to express F. The transitional step, v is a virtual step a virtual state, as G might not be sufficient to sustain continuity [20].

F^e, on the other hand, generates mechanical stresses on the volume. Stress- strain behaviour of neo-Hookean type with Cauchy stress, σ = [λ ln(det (F^e)) − μ]I + μF^e. (F^e)^t , is assumed. Where, λ and μ are elastic Lame constants and I is the second order identity tensor [10].

What is this virtual or intermediate stage? In classic non-linear elasticity, the Cauchy-Green Tensor, C = F^t.F is a useful tool for measuring fluctuations in angles and lengths. In the presence of growth, F^g maps the tangent space at each point of initial configuration to the tangent space of the virtual stress-free state. So, we have that C^g = (F^g)^t . F^g However, the union of these tangent spaces forms a tangent bundle that defines the intermediate configuration, but this configuration is not clearly

defined. By considering, the Weitzenbock manifold instead, we have $\tau(F^g) = F^{g-1}\text{skw}(\nabla F^g)$ where skw () defines the skew-symmetric part of a tensor (). Hence, the intermediate configuration used in finite elasticity can now be formally defined as a Weitzenbock manifold with torsion tensor, $\tau(F^g)$ [10].

Finite growth, therefore, shows that the growth tensor, which represents rates of change, is intrinsically dependent on mechano-chemical cues.

Taber [85] explored the biological growth process in arterial walls in response to mechanical stimuli. He studied the stress-modulated growth in the aorta using a theoretical model of a thick-walled tube composed of two pseudo elastic, orthotropic layers representing the intima/media and adventitial layers [85]. The application of the Volumetric Finite Growth model resulted in reasonable agreement with published data for global and local growth of rat aorta. Based off Taber's [85] work, Rodriguez [86] proposed a model for the realistic predictions of mechanical response of coronary arteries. Similar to Taber [85], the volumetric growth was induced by fluid shear stress in the intima and the local wall stress in arteries with patient-specific geometry and loads. Although his application to the patient-specific right coronary artery was not successful due to the lack of necessary information, this study was able to apply the volumetric finite growth model to the stenotic process of an idealised geometry induced by non-uniform shear stress distribution. It was observed that the luminal radius reduced due to the shear stress (1.5 Pa) being below the equilibrium value (2.5 Pa). Similarly, the wall thickness was also observed to reduce because the hoop stress was lower than the equilibrium value, thus, producing negative radial growth [86].

C. Constrained Mixture theory

One of the main limitations of the volumetric finite growth theory is the assumption that the soft tissue volume is made of one type of material which is split into material points. However, that is not true in biological systems where tissue is made up of different cell types and extracellular matrix. These tissue constituents can turnover at different rates and possess different stress-free configurations that evolve during growth and remodelling while being constrained to deform as a continuum within the mixture [12]. The continuum theory of mixtures is a logical starting point for modelling. The deposition of new material occurs at the current configuration, hence, a newly deposited volume will experience a different stress and strain than the previous volume, even if it's of the same constituent material [12]. Figure 2.3. illustrated the constrained mixture theory. Consider the mass balance for a mixture of $\alpha \equiv$ k = 1, 2, 3, 4, ..., N structurally significant constituents.

We have;[10]

$$\frac{\partial \rho^k}{\partial s} + \nabla\left(\rho^k v^k\right) = m^k \qquad (2.2.10)$$

where, ρ^k - the spatial mass density

v^k - velocity

m^k - net rate of mass density productive (or removal)

ρ^k, v^k and m^k depend on many chemical and mechanical factors including stress and the growth and remodelling time, s. The assumptions used to develop the constrained mixture theory for growth are;

(i) individual constituents can have separate natural, stress-free configurations but are constrained to move with the mixture as a whole, i.e. $x^k \equiv$ x

(ii) growth and remodelling are typically slow relative to rates of mechanical loading, i.e.

$\dot{x}^k = v^k \equiv v \approx 0$

net rate of mass production (or removal) can be modelled via a multiplicative decomposition,

i.e. $m^k(\tau) = m^k q^k$ where, $m^k > 0$ is the true rate of mass production and $q^k(s, \tau) \in [0, 1]$ is a survival function that tracks that part of the constituent produced at growth and remodelling time $\tau \in [0, s]$ that remains at current time, s. Therefore, we have a mass balance [10]

$$\rho_R^k(s) = \rho_R^k(0) Q^a(s) + \int_0^s m_R^k(\tau)\, q^k(s, \tau)\, d\tau \qquad (2.2.11)$$

where, $\rho_R^k(s) = \sum_{k=1}^{N} \rho_R^k(s)$

R refers to quantities defined per unit reference volume

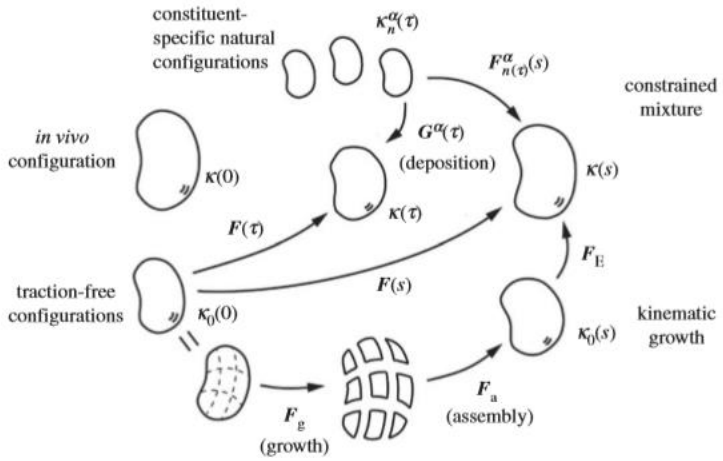

Figure 2.3: Schematic drawing of evolving configurations of importance in both a theory of finite kinematic growth (bottom portion) and a constrained mixture theory (top portion).

Take note of the common reference $\kappa_0(0)$ and current $k(s)$ configurations in Figure 2.3. According to kinematic growth theory, infinitesimal stress-free portions of the body grow independently through the transformation F^g, without necessarily leading to compatible growth. A continuous traction-free body is provided by an elastic assembly transformation F_a, which usually results in residual stress. The current configuration of interest is finally obtained through an elastic load-dependent transformation $F^e = F_E F_a$ where the stress field is determined by the elastic portion of the deformation. On the other hand, in the constrained mixture theory, the elastic stress within a constituent is determined by the constituent-specific deformation $F_n^\alpha(\tau)$ from an individual stress-free configuration. It is easy to demonstrate that $F_n^\alpha(t)(s) = F(s)F^{-1}(\tau)G^a(\tau)$, where $G^a(\tau)$ is a tensor that accounts for cells depositing new extracellular matrix under stress when incorporating it within stressed extant matrix. The tensor is known as a deposition stretch. Both approaches call for multiplicative deformations: one in terms of the deformation inherent in each constituent when it is integrated into existing tissue, and the other in terms of the specified growth of stress-free elements [10].

Q^k(s) ∈ [0, 1] is similar to q^k(s, τ) but for constituents produced at or before time 0 and have property, Q^k(0) = 1 similar to q^k(τ , τ) = 1

To avoid using the full mixture relation and instead use the classical equation of linear momentum balance, we suppose that Cauchy stress can be obtained from a rule of mixtures relation for stored energy per unit reference volume.; $W_R = \sum W_R^k$. Therefore, we have an expression for stress that is consistent with the standard constitutive relation of finite elasticity;[10]

$$\sigma = \frac{2}{\det(F)} F . \frac{\partial W_R}{\partial C} . F t - pI \quad (2.2.12)$$

where, p - Lagrange multiplier that enforces compressibility during transient motions.

We can now mathematically define a constitutive form for energy stored in each constituent due to to its deposition and each individual deformation as [10]

$$\rho W_R^k(s) = \rho_{R(0)}^k Q^a(s) \widehat{W}^k \left(C_{n(0)}^k(s)\right) + \int_0^s m_R^k(\tau) q^k(s,\tau) \widehat{W}^k(C_{n(\tau)}^k(s)) d\tau$$

where, $\widehat{W}^k$- stored energy functions depending on constituent-specific Right Cauchy-Green tensors, $C_{n(\tau)}^k(s) = (F_{n(\tau)}^k(s))^t . F_{n(\tau)}^k$ k(s)) , for each structurally relevant constituent, and

$(F_{n(\tau)}^k$(s)) - deformation gradient that each constituent, k, experiences relative to its own natural configuration, κ_n^k(τ) which can evolve and is simply denoted by n(τ).

We deduce that the deposition stretch functions as an internal variable in the constrained mixture theory, and mass production (and removal) functions reflect rates of change. The three constitutive functions; m_R^k (τ)-mass production, q^k (s, τ)-mass removal and $\widehat{W}_k(C_{n(\tau)}^k(s))$ -mechanical properties of existing mass, are required. Therefore, making this theory better placed to model tissue growth more accurately as this microstructurally motivated model is better capable of capturing many of the underlying mechanisms of growth and remodelling.

The Constrained Mixture Model has been used to model growth and remodelling induced by changes in blood pressure, blood flow and axial length in adult arteries [87]. Alford's [88] study, identified and quantified vascular cells and matrix responses and mechanisms in various mechanical environments. Whereas various studies investigated how varying mechanical perturbations drive growth and remodelling to approach mechanical homeostasis [89][90][91]. Hypertension has also been modelled successfully using the Constrained Mixture Method in both adult arteries [92] and in developing mouse [87] and rat [22] abdominal aorta.

2.3.2 Agent Based Modelling (ABM)

ABM, also known as Individual based modelling (IBM), is a computational method that predicts higher level emerging patterns by simulating the interactions of autonomous entities (i.e., agents, or individual cells) with their local environment and one another [21]. ABMs, as opposed to continuum models, provide a more accurate depiction of cellular systems by implementing a well-defined set of rules that govern the behaviour of each of the agents [25]. These rule sets may be deterministic or probabilistic, and they may be dependent on external factors (relating to the effects of the immediate surroundings and neighbouring agents) as well as internal variables (pertaining to the intrinsic dynamics of the agent) [27][28]. Higher-level patterns are produced by simulating the interaction of a collection of agents reacting to nearby agents and local conditions, and the investigation of more

complex behaviour is made possible by the incorporation of various agent types [21]. As a result, ABMs resemble biological tissues, whose functions are the consequence of individual cell behaviours that combine to produce tissue-level patterns that are constructed top-down. With this bottom-up approach, the system's behaviour will automatically emerge from the imposed fundamental rules, reducing the requirement for a full understanding of the system [25].

ABM offers a novel and appealing method for researching and modelling intricate mechano-chemo-biological processes at the cellular level [22]. At the molecular level, complex mechano-chemo-biological processes dictate cell-mediated tissue adaptations. Such biological complexity should be able to be included at multiple scales in increasingly complicated models [23]. Agent-based models are particularly helpful in the creation and preliminary profiling of theories regarding the ways in which tissues modify their patterning through growth, adaptation, or structural remodelling [21]. Using a set of rules developed directly from data, ABM represents individual cells as agents capable of exhibiting realistic biological characteristics. Time and space are handled separately, and interactions among hundreds or thousands of agents can result in emergent tissue-level responses. Thus, the strength of ABM resides in its capacity to simulate biologically meaningful stochasticity and to represent individual biological cells as well as heterogeneous cell-cell interactions [23]. This stochasticity that ABM accounts for, allows for a non-deterministic framework.

Several research groups have developed ABM frameworks, employed at different spatial and temporal scales, of physiopathology in the vasculature. They have attempted to gain insight into the mechanisms that drive multiscale remodelling by predicting the vascular response to variations in their mechanical environment and genetic expression [25]. To represent the underlying mechanisms of the response to endovascular treatments or surgical interventions and to convey the complex character of vascular diseases, a number of multiscale models have been put forward. The development of atherosclerotic plaques [29][30][31], the processes of restenosis after endovascular treatments [32][33][34], and vein-graft remodelling [35][36] are some of the more significant applications of the ABM to date.

More relevant to this study has been the model application to the vascular remodelling process, more specifically, the arterial response to changes in chemicals, mechanical stimulation, or growth factors [23][24][25]. Thorne submitted that in order to study large vessel adaptations, when paired with proven continuum models, ABMs, provide multi-scale models of tissue-level phenomena. The ABM would be useful in modelling the cell-level activity while the continuum model would reflect the tissue-level pattern. It is necessary to make sure that each model accurately captures the best available data at the appropriate scale in order to couple agent-based and continuum models, and that models are consistent under baseline conditions.

Towards this end, Thorne explained how an ABM of SMC and EC responses to mechanical stimuli in a large artery was developed and verified. His study consisted of a proposal of a refined ruleset based on a broad literature search and the development of a new scoring system to assign confidence in the rules. Furthermore, a parameter sensitivity study was carried out. The verification process of the ABM and its consistency with the continuum-level model was carried out by studying the simulated mouse aorta response to homeostatic conditions, as well as transient and sustained increase in pressure. The simulated responses were dependant on the altered cellular production of six key biomolecules (TGF-β, PDGF-AB, ET-1, NO, MMP1, MMP2 and MMP9), which in turn control the turnover of intramural cells (SMC) and extracellular matrix (Elastin and Collagen). These events are thus responsible for changes in vessel wall morphology.

The developed ABM was found to be responsive to increased intramural wall stress in hypertension, insensitive to brief spikes in blood pressure, and suitably stable under homeostatic conditions [23]. The results of this study were compared to results of the well-established continuum model, CMM. Whereas CMM allows for the prescription of lumped parameter models based on fluctuating strains and stresses that describe local cell-mediated production and turnover, ABM addresses the discrete cell-level activity and production of diverse molecules in a non-deterministic framework [22]. Therefore, CMM and ABM account for different, although complimentary, methods of simulating the intricacy of tissue-level, cell-mediated adaptations [23].

Beyond that, Keshavarzian [24] proceeded to investigate the interaction of bio-chemo-mechanical components in blood vessels and their function in preserving homeostasis. A computational framework was created in Java™ to enable quick and reliable coupled ABM-FEA simulation of blood vessels. The base code for the ABM and the commercial FE package ANSYS (ANSYS Inc., Canonsburg, PA) for FEA simulations were sourced from the REPAST Simphony libraries [40]. This computational approach was able to capture the response of blood vessels to changes in blood pressure as well as micro-level changes in growth factors, proteases, and other signalling molecules by coupling a continuum-level model (FEA) to a cellular-level model (ABM) [24]. An implementation on a 3D porcine left anterior descending artery (LAD) was made. This ABM was an expansion upon the 2D mouse aorta model [23] created in Netlogo [41]. The ABM module modifies this environment for 3D lattice-based biological simulations while implementing the REPAST Simphony libraries [40]. The model was built using histology information from a pig hypertension model. This study revealed details about the LAD's structure, starting cell density, and quantity of structurally essential ECM proteins [39]. As a result, a suitable collection of agents and rules were created. The model was able to recover from brief spikes in blood pressure and was stable under normotensive settings, as demonstrated by the simulations. According to the sensitivity tests, the model is particularly sensitive to changes in the concentration of growth factors that influence cellular proliferation and control the composition of the extracellular matrix, primarily collagen [24].

2.4 Comparative Medicine

Literature searches reveal limited blood vessel growth and remodelling ABM studies carried out on rat species [22] and porcine species [24]. In the development of growth and remodelling models of rat and porcine blood vessels, experimental data is considered in order to obtain different parameter values for the ABM ruleset. However, due to the gap in experimental work and biological modelling work, a comprehensive and rigorous list of parameter values is difficult to develop. This difficulty arises from literature being incomparable due to differences in species being studied, the type of blood vessel being studied and differences in experimental procedure.

This study aims at modelling aortic growth in human toddlers. Like the rat and porcine species case, comparable experimental studies could not be obtained from literature to create a rigorous list of parameter values in order to develop the agent-based growth model rule set for human babies. To alleviate this challenge, a comparative medicine approach is used to build the model.

In order to gain a deeper understanding of the mechanisms underlying both human and animal disease, comparative medicine is commonly characterised as a field which links and takes advantage of the biological similarities and differences among animal species [42]. In an attempt to advance treatment for both human and animal diseases, comparative medicine serves as a link between both fields [43]. Characterising genes and proteins, studying anatomical and physiological processes, and

characterising normal and diseased states in a range of animal species, are all aspects of basic biomedical research. The understanding of these identical processes in humans is then based on this knowledge [44]. Animal research remains essential to the advancement of biomedical research [43].

Because of their many anatomical and physiological parallels to humans, laboratory rats and mice provide useful animal models for biomedical research and comparative medicine studies. Similarly, each of the three species—rats, mice, and humans—has about 30,000 genes, of which 95% are shared [45][46][47][48]. Rodents have several advantages, such as their small size, low maintenance requirements, short life span, and wealth of genetic resources [44].

For cardiovascular research, where their larger size is advantageous, particularly for enabling surgical operations and other sorts of testing, rats are frequently the selected rodent model. Rats make good animal models for the study of obesity, diabetes, and cardiovascular disease because several different strains of the rodent have been engineered to mimic the complicated nature of these conditions in humans [49][50]. The rodent model of choice ultimately comes down to whatever species best mimics the signs and progression of the disease in humans. Selecting the right model is especially important from the perspective of translational medicine because a lot of money is wasted on studying medications and treatments that eventually fail at different phases of pre-clinical and clinical trials. This is due, in part, to the fact that human outcomes are not always accurately reflected in animal trials [44].

Because of their similar anatomy and physiology to humans, as well as the fact that the porcine genome is three times closer to the human genome than the mouse genome, pigs provide an excellent animal model for studying human health and disease [51]. The biomedical world has more recently accepted naturally occurring and genetically modified pig models as animal models for human health and illnesses. The fundamental knowledge of the biology behind the genes and proteins involved in human health and disease has been substantially improved by the classical rodent models, but because these models are not very good at simulating some human diseases, their applicability is limited, and porcine models may work better [52]. Pigs are excellent models for studying conditions associated with the cardiovascular, gastrointestinal, and pancreatic systems because of their similarities to humans in their morphology and the roles they play in the body [52].

This study takes advantage of the backing provided by comparative medicine to build a growth model for human babies by first developing the growth model in the rat species and the porcine species. These studies are used as vital steps to eventually create a growth model for the CoA patient specific case.

Chapter 3: METHODS

3.1 Coupling Overview

To successfully model the growth process of the aorta, the key components involved must be captured systematically. As described in Chapter 2, growth is a mechano-biochemical process. However, the mechanical and biochemical processes happen at different spatial-temporal scales. Thus, the growth process can be broken down into 2 parts i.e. (i) Mechanical stimuli and (ii) Biochemical response process. This breakdown allows us to capture both processes in more simplified and manageable models at their respective spatial-temporal scales. The mechanical stimuli, as discussed in chapter 2, is reflected by the blood flow (haemodynamics) acting on the vessel wall which happens at tissue level and over a few seconds. While the biochemical response process is comprised of the proliferation and apoptosis of intramural cells, as well as production and removal of various growth factors and growth hormones occurring at the cell level and can take anywhere from a few seconds to more commonly a few months or years in order to have observable changes.

These two components are modelled by CFD and the ABM respectively. The coupling of these components works harmoniously to model this multi-scale process of growth. The CFD models haemodynamics of a given vessel geometry with specified boundary conditions to give an output of mechanical parameter values, and the mechanical parameters are the input variables that stimulate/drive the biochemical processes, modelled by the ABM, to give a new geometry. This new geometry can then be fed back into the CFD model to obtain new mechanical parameter values.

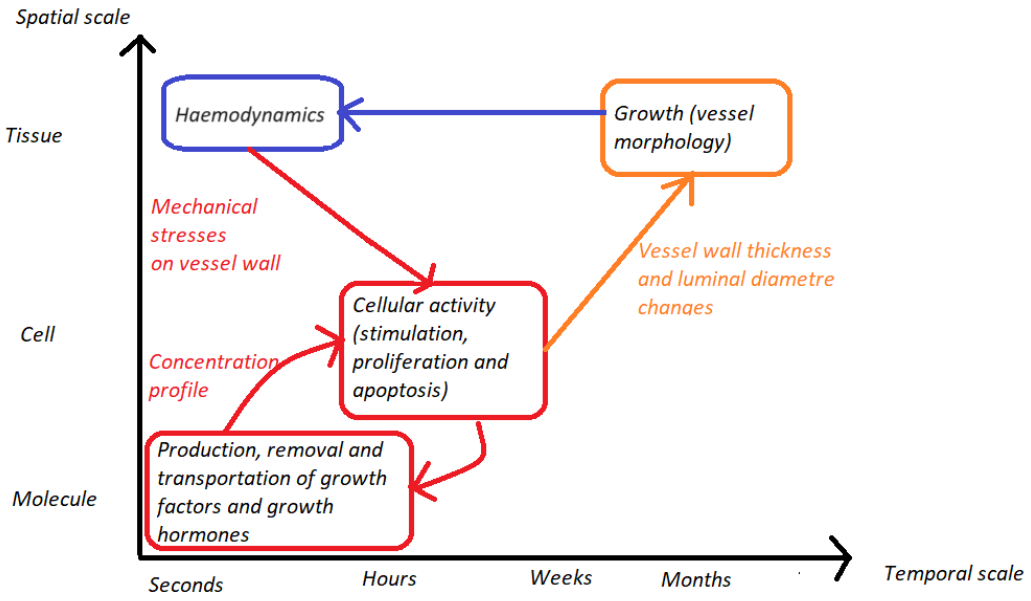

Figure 3.1: Schematic representation of the muti-scale framework of vascular growth at different spatial-temporal scales. Growth (in orange) is modelled by the coupling of the Continuum model (in blue) and the ABM module (in red). The modules receive inputs (arrow inwards) and generate suitable outputs (arrow outwards).

3.2 Computational Fluid Dynamics (CFD)

As shown in Figure 3.1, at the tissue level of this multiscale framework, the vessel experiences blood flow, responsible for the mechanical stresses to the vessel wall that stimulate growth. The blood flow simulation, represented by the process encapsulated in blue in Figure 3.1, has been studied by collaborators in the PROTEA project. Therefore, a concise description of this work will be discussed here. This thesis focuses on the biochemical response process of growth (represented by the processes encapsulated in red and orange in Figure 3.1) and thus the output of the haemodynamic simulation is of great interest.

Geometry data of the patient's aorta was obtained through CT scan and image segmentation of the region of interest was carried out using SimVascular, an open-source modelling toolkit. Further, the geometry volume was discretised by generating a mesh using ANSYS ICEM CFD (version 19.2) commercial package.

The patient's flow data (i.e., velocity and pressure) was extracted from the Echo of the patient. These flow metrics were necessary in defining the velocity and pressure boundary conditions at the inlet and outlet of the vessel for the haemodynamic simulation.

The CFD package, OpenFOAM (version 6) was then used for pulsatile blood flow simulation with boundary condition settings of steady state inlet mass flow and mass flow with zero pressure at the outlet. The wall was taken as being rigid with a non-slip condition.

The CFD simulation was able to output a visual representation of flow as shown in Figure 3.2 below and an output point data csv file which included coordinate data and its associated pressure and wall shear stress vectors for each discretised cell.

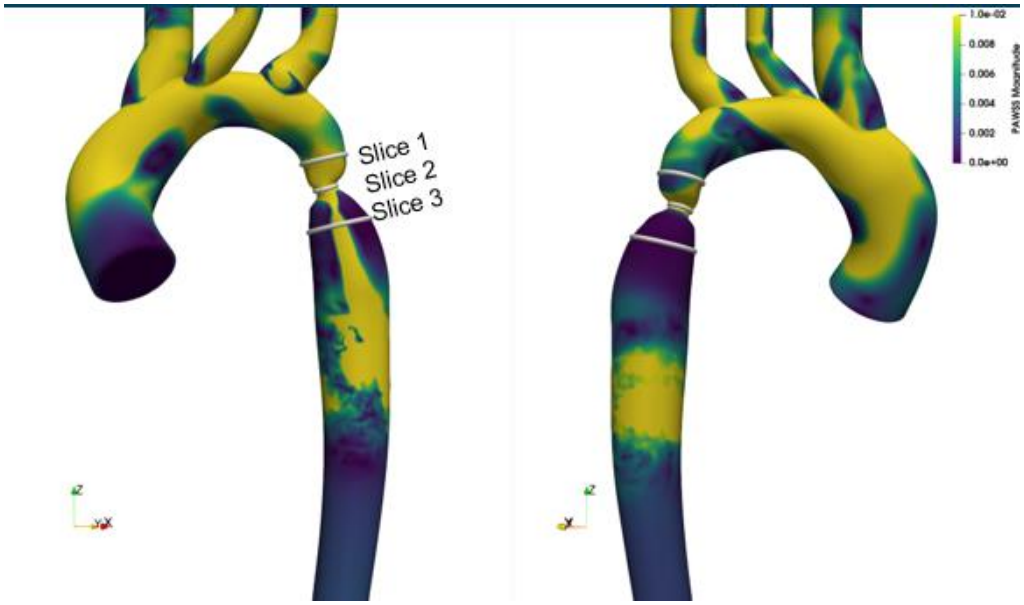

Figure 3.2: A screenshot of the visual output of the CFD models.

Post-processing included:

1. Taking 2D slices across the centreline along the length of the 3D aorta geometry. Thereafter, extracting the diameter of each slice.

2. Taking the magnitude of the WSS of each discretised cell along the length of each 2D slice and then calculate the average along that line.
3. Taking the average pressure between the systolic and diastolic for each pulse and then calculate the average over several pulses.

   Refer to Appendix 3.2 for the full table of post-processed CFD results.

3.3 ABM Pre-processing

The ABM was designed and employed to represent the molecular and cell aspect of this multiscale growth framework.

(1) In order to reduce the complexity and save on simulation time of the ABM, a decision to take 2D disc slices along the length of the 3D aorta was made. Hence, the geometric data and mechanical parameter values for each disc were considered at any given time.

(2) In the biochemical process, the thickness of the vessel wall is vital in determining the number of cells to be individually represented in the ABM environment. CFD in its simulations is limited to the blood flow within the lumen of the vessel with the inner (endothelial cell) layer represented by a rigid wall. In this way the thickness of the vessel wall information is lost. This then called for an assumption to be made to determine the vessel wall thickness. With the reference to a literature derived healthy aorta, the thickness was assumed to be proportional to the luminal radius at each location along the length of the aorta. The luminal radius was obtained from the luminal area given from the CFD output.

$$radius_{lumen} = \sqrt{\frac{Area_{lumen}}{\pi}}$$

(3) CFD models pulsatile haemodynamics at a temporal scale of a few seconds per heartbeat. However, growth is attributed to consistent blood flow pattern observed over more than a few hours. This allows for the homeostatic negative feedback loop to be initiated if the blood flow pattern is simply a variation experienced over a short period of time, otherwise, the pathological process is observed. An average blood pressure was therefore used from the CFD, both the systolic and diastolic pressure average and an average over multiple heartbeats for each slice.

Consequently from (1) and (2), the blood pressure(P) observed in the CFD was translated to the circumferential pressure (σ_θ) felt by the individual cells, thus kickstarting the biochemical processes.

$$P = P_{kinematic} * 1060\ Kg/m^3$$

$$\sigma_\theta = \frac{P * radius_{luminal}}{wall\ thickness}$$

(4) Similarly, the wall shear stress was observed over multiple heartbeats. However, unlike the blood pressure, the WSS biochemically only stimulates the cells on the intima wall (endothelial cells). Therefore, the average of the magnitude of the WSS of each discretised cell along the length of each 2D slice was taken.

$$WSS = WSS_{kinematic} * 1060\ Kg/m^3$$

3.4 ABM Solver

NetLogo is an open source, multi-agent programmable modelling environment. It allows the user to either tailor models in its library or create new models altogether. A model was created from scratch to carry out this study in NetLogo (version 6.2.0).

The model was constructed based on the information provided by the user regarding geometric features of the artery slice (luminal radius and wall thickness), composition of each layer i.e. the intimal and medial layers (note that the adventitial layer was discarded because not enough data in literature was found to support its importance in the growth process), the size of various cell types. Here, the animal cell was represented by a pixel area of $1.0 * 10^{-6}\ cm^2$ in the ABM. This information was provided by using the graphical user interface (GUI).

Figure 3.3 shows the model construction process.

Graphical Representation of a 2-D Cross-section of Artery in NetLogo.

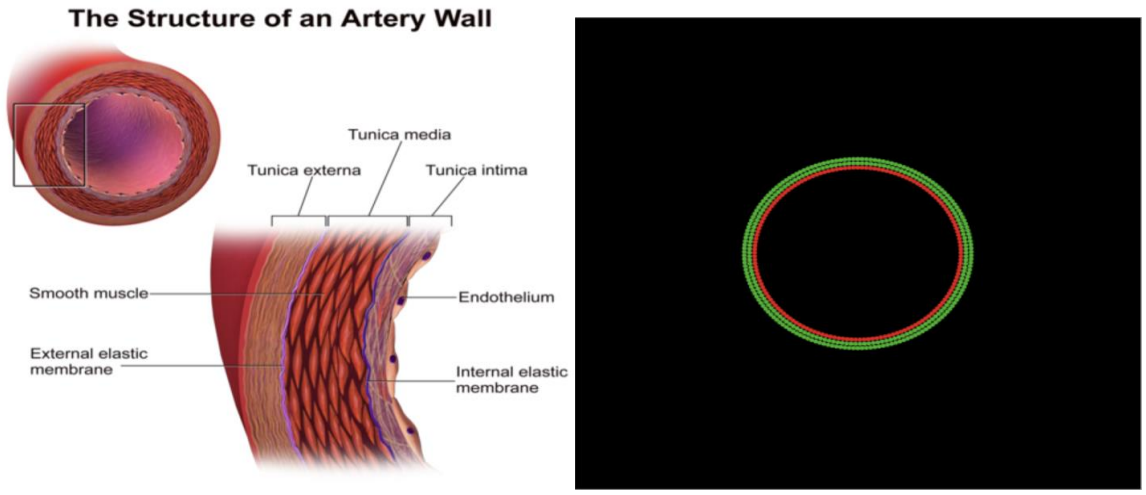

Figure 3.3: This depicts the translation process of the arterial structure to the ABM in NetLogo. The circles represent agents where ECs are red, and SMCs are green.

As the model aims at predicting arterial growth in response to alterations in circumferential pressure and WSS, the rules included in the model were focused on the regulation of SMCs, growth factors and growth hormones clearly laid out in Tables 3.1 and 3.2. The extracellular matrix composed of collagen and elastin. However, elastin turnover was assumed to be insignificant under normal condition given that its half-life is 40 years [94]. Collagen was also assumed to be insignificant to the growth process as its deposition pattern is vital for the material changes in the vessel walls in the remodelling process. The rule-set was obtained by considering the studies of Hayenga [22], who focused on the rat species, and Keshavarzian [24], who focused on the porcine species. Data regarding the rules gleaned from this literature was translated into mathematical equations and systematic language that could be used in NetLogo. The agents and rules-set remained the same from species to species given that comparative medicine was taken advantage of by choosing species that had a similar genetic make-up, biochemical processes, and vessel structure to that of human beings. Table 3.1 provides the complete and detailed list of the rules used in the ABM development in this study, while Table 3.2 in Section 3.7 provides the parameter values of the rules specific to each species.

Table 3.1: A summary of the rules governing the SMC that are induced by circumferential stress, σ_θ, and those governing the EC that are induced by the WSS, τ_w .

Behaviour	Importance	Literature-derived Rule	Literature References
SMC Proliferation chance	SMC production	SMC proliferation chance = 100 in -1.45E-9 (PDGF-AB + 8.0E+4 /cell/6h)	[22][24][67][68][69]
SMC Apoptosis rate	SMC death	SMC apoptosis chance = 100 in 71020 /cell/6h	[24]
PDGF-AB *(induced by circumferential pressure, σ_θ, on SMC)*	Growth factor in SMC production	$PDGF-AB_{induced\ by\ \sigma_\theta}$ = 4.79E-7 (σ_θ) + (-4.17E-5) pg	[22][24][70][71]
NO *(induced by WSS, τ_w, on EC)*	Stimulates growth hormone secretion	$NO=\begin{cases} 0 & for\ \tau_w < 0 \\ 0.5 & for\ 0 < \tau_w < 1 \\ 0.272\ (\tau_w) + 0.22 & for\ \tau_w = or > 1 \end{cases}$	[22][24][72]
PDGF-AB *(induced by WSS, τ_w, on EC)*	Growth factor in SMC production	$PDGF-AB_{induced\ by\ \tau_w}$ = *M (δ + α (1 - $e^{-\kappa\tau_w^n}$))* *where,* *M = max rate = 0.078 pg/cell/6hrs* *δ = 0.15, α = 0.84, κ = 0.42, n = 1.24*	[22][24][73][74]

NetLogo, was programmed to output a visual representation of the agents that are updated after each temporal unit called a tick by way of update formulae. In our study each tick represented a 6-hour period in nature. The expected output, growth, was quantised by the vessel wall thickness.

During each simulation of growth, the number of SMCs is updated after each tick through a counter and a graph is plotted i.e. number of SMCs against ticks. Based on the number of cells the thickness is calculated/updated using the equation below.

$$Thickness = radius_{\ aorta} - radius_{lumen}$$

$$= \sqrt{\frac{Area\ of\ vessel}{\pi} + radius_{lumen}^2} - radius_{lumen}$$

By earlier assumption, $Area\ of\ vessel = number\ of\ SMCs * \ 1.0 * 10^{-6}\ cm^2/SMC$

Each ABM simulation is run to model 6 months of growth in nature and a graph plotted reflecting the number of SMCs and thickness against time during that 6-month time period (i.e. 730 ticks).

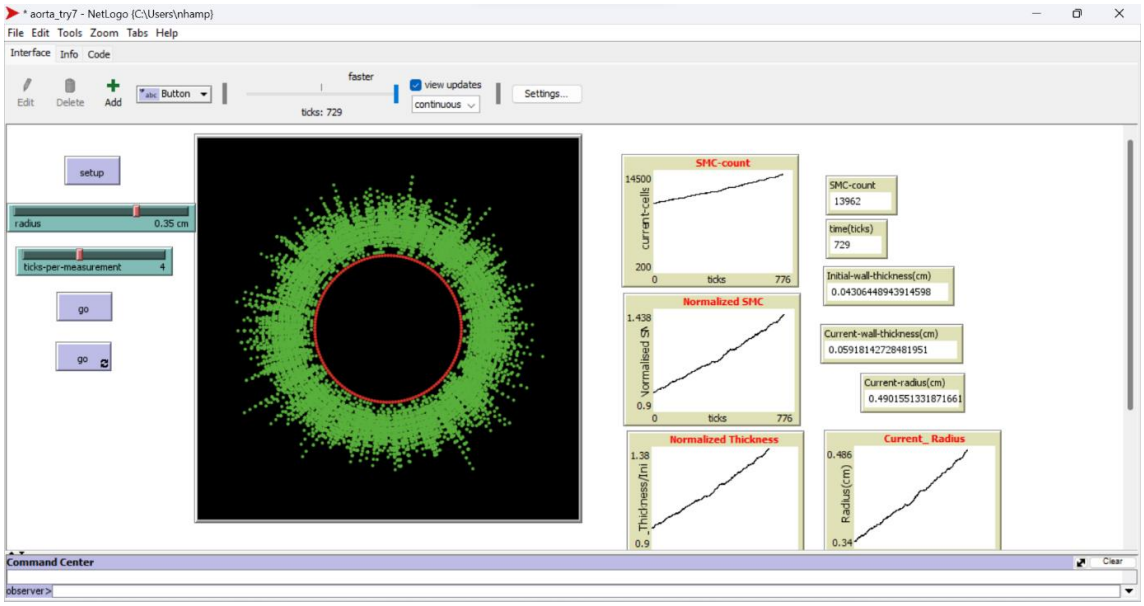

Figure 3.4: GUI in NetLogo showing the visual representation of the ABM for a healthy 18-month-old toddler. The ECs are represented by red circles while SMCs are green. It also shows various output graphs that are updated after every 4 ticks over a 729-tick period (6 months in nature).

It is important to note that 5 simulations were run for each disc and average calculated in order to capture and account for the non-deterministic/stochastic nature of the ABM.

As supported in Chapter 2.4. The ABM was gradually built up by considering the rat aorta, the porcine carotid artery, the healthy 18-month toddler's abdominal aorta and finally the patient specific case. Literature derived geometric and material input metrics were used for the rat abdominal aorta growth ABM, porcine carotid artery growth ABM and healthy 18-month-old toddler abdominal aorta growth ABM. However, in the case of the 18-month-old patient, geometric and material input metrics were obtained from the CFD post-processed data (by *Jie Wang*).

3.5 ABM post-processing

Growth is quantified by the change in thickness of the vessel wall from the ABM. A growth rate was obtained using the formula below.

$$Growth\ rate = \frac{Average\ Thickness_{at\ 730\ ticks} - Thickness_{initial}}{Thickness_{initial}}$$

As stated in Chapter 3.3, the ABM can only model changes in thickness, however, the CFD is only able to make use of the luminal radius of the vessel. Therefore, a change in thickness is captured by a proportional change in radius. This new radius is then used as an input to the CFD in order to obtain a new 3D geometry and thus run haemodynamic simulations for the grown aorta geometry. Thus, completing a coupling iteration.

The aim of this study is to build a reliable ABM to predict growth of the aorta in CoA patients. To this end, the ABM was progressively developed and studied for species with more experimental literature for the model validation process. Although these species had more literature on cardiovascular experimentation, a broad literature search produced no results for data specifically on aortic growth. However, this search revealed that the Body Surface Area ((BSA), which takes height and body size

into consideration, has been shown to be correlated with aortic diameter [53]. Numerous studies have concentrated on developing nomograms, which are already included in echocardiography guidelines, for the purpose of predicting aortic diameter based on BSA [54]. BSA versus aorta Diameter nomograms by age group and a formula for expected aorta size by age, gender, and BSA were generated using linear regression models [55]. Wolak, concluded that BSA was directly associated with the thoracic aorta dimension. Further, the size of the Ascending Aorta showed strong correlations with age, age squared and BSA [56].

With this revelation and availability of more weight experimental data for each species, the BSA was calculated where vessel diameter information was scarce to validate the ABM predicted growth trends.

BSA was defined as; $BSA = \frac{4 * weight(kg) + 7}{90 + weight\ (kg)}$

3.6 Statistical Tools

Throughout this study two statistical tools were used.

1. Standard deviation (SD) was useful to describe the dispersion of the mean value of the change in thickness after each repeat simulation (i.e. i=1,2,3,4 or 5) for each 2D slice.

$$SD = \sqrt{\frac{\sum_{i=1}^{5} Thickness_{at\ 730\ ticks,i} - Average\ Thickness_{at\ 730\ ticks}}{5}}$$

2. Percentage difference was also used to measure how far off the model was from literature derived experimental expected values.

$$Percentage\ difference = \frac{Parametre_{model} - Parmetre_{Literature}}{Parmetre_{Literature}} * 100\%$$

3.7 Species-Specific ABM

To achieve species specific growth, the vessel dimensions were adjusted for each species as is tabulated in Table 3.2. Conversely, the agents and rules-set remained the same from species to species given that comparative medicine was taken advantage of by choosing species that had a similar genetic make-up, biochemical processes, and vessel structure to that of human beings. Table 3.1 in Section 3.4 provides the complete and detailed list of the rules used in each species while Table 3.2 provides the parameter values of the rules specific to all species. The development of the patient specific growth ABM was executed by successively scaling up the species-specific ABM.

Table 3.2: Summary of species-specific ABM input variables and their respective values.

Input Variable	Rat abdominal aorta	Porcine carotid artery	Healthy toddler abdominal aorta	Patient-specific descending thoracic aorta			
				Slice 1	Slice 2	Slice 3	Slice 4
Outer diameter (cm)	0.05212	-	-	-	-	-	-
Luminal diameter (cm)	0.04600	-	0.700	-	-	-	-
Luminal radius, a (cm)	0.02300	0.044121	0.350	0.323	0.155	0.451	0.527
Initial vessel wall thickness, h (cm)	0.00306	0.011623	0.043	0.040	0.019	0.055	0.064
# of ECs	153	153	153	153	153	153	153
# of SMC	319	3485	9900	8500	1900	16500	22300
WSS (Pa)	8.8	7.42	7.42	3.191	58.550	2.368	2.164
σ_θ (kPa)	100	50.486	83.023	109.978	100.443	103.970	121.773

Chapter 4: RESULTS & OBSERVATIONS

4.1 Species- Specific ABM

4.1.1 Rat abdominal aorta

The rat abdominal aorta ABM was studied by considering growth from birth to adulthood of the rat. Rats on average have a period of 14 weeks of growth from birth to adulthood, after which they maintain a steady weight. Therefore, the rat growth ABM simulation was run for only about a 14-week/ 100-day period (400 ticks). The amount of growth was noted at different ages and compared against the expected growth from experimental literature.

Table 4.1: Table summary of the output ABM predicted radius for the rat abdominal aorta after growth.

Age	**Literature Derived Expected Radius (cm)**	**ABM Simulation 1 (cm)**	**ABM Simulation 2 (cm)**	**ABM Simulation 3 (cm)**	**ABM Simulation 4 (cm)**	**ABM Simulation 5 (cm)**	**ABM Average radius +- SD (cm)**	**% Difference (%)**
5 Weeks (Beginning of puberty)	0.035	0.02300	0.02513	0.02396	0.02460	0.02423	0.02426 +- 0.00032	30.7
10 Weeks (End of puberty)	0.035	0.02590	0.02826	0.02637	0.02771	0.02753	0.02720 +- 0.00073	22.3
14 Weeks (Adult)	0.035	0.02570	0.02920	0.02744	0.02847	0.02704	0.02765 +- 0.00074	21.0

(a) (b)

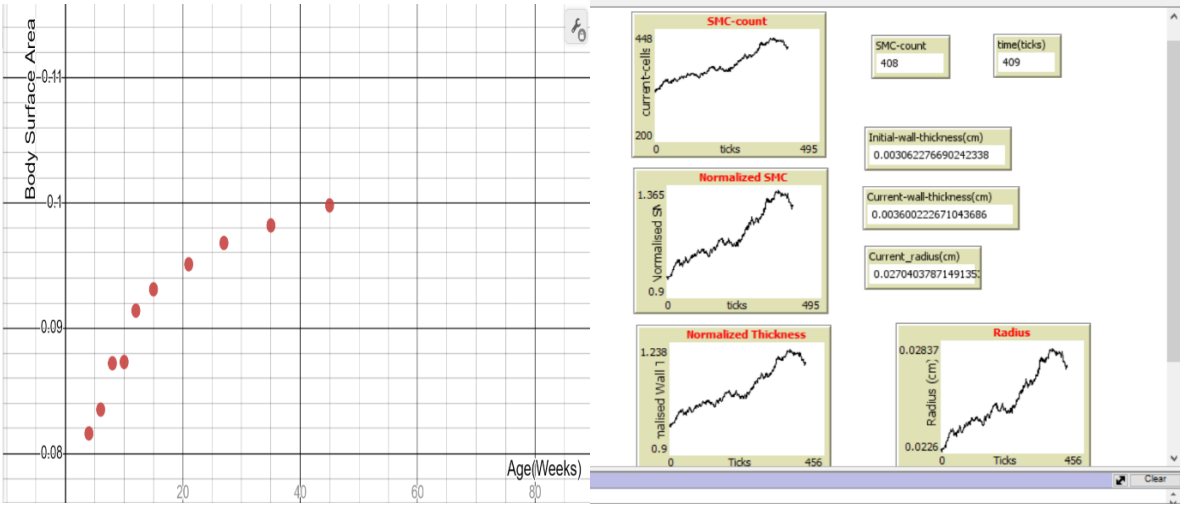

Figure 4.1: (a) Growth curve obtained by considering the BSA against the age of the rat in weeks. (b) A NetLogo simulation output showing the various graphs including the trends of the number of SMCs (SMC-count) against time (in ticks), the normalized number of SMCs against time (in ticks), normalized vessel thickness against time (in ticks) and the luminal radius against time (in ticks). Output windows reflecting the number of SMCs, time (in ticks), initial and current wall thickness, and radius, at any given time are also shown.

The growth curve generated by the BSA of the rat species compared to that generated by the vessel thickness and luminal radius prediction by the ABM shows similarities in shape as can be noted from Figures 4.1 (a) and (b). This is a useful validation step for the rat abdominal aorta growth ABM. In addition, a further study of the growth rates showed that the rate increased during puberty and reached peak rate at puberty and then begun to reduce as the rat aged into adulthood. This is consistent with the general understanding of growth in animals. The ABM predicted growth rate averaged throughout the 9-week observation time was 0.202 compared to the literature expected growth rate of 0.522, a 61% difference.

Further validation is carried out by considering, in more detail, the comparison of the predicted luminal radius growth of the ABM against the expected growth from literature derived experimental studies. Consider Table 4.1. First, it is important to note that literature with regard to experimental studies of rat abdominal aorta luminal radius were not exhaustive. A literature search produced the abdominal luminal radius of the rat in its infancy and adulthood phases of life, therefore the initial value used in this study is that in its infancy and the expected value after growth is that in its adulthood. When compared with the predicted luminal radius after growth at various stages of life, as expected, greater accuracy was observed in the adulthood comparison with a 21% difference.

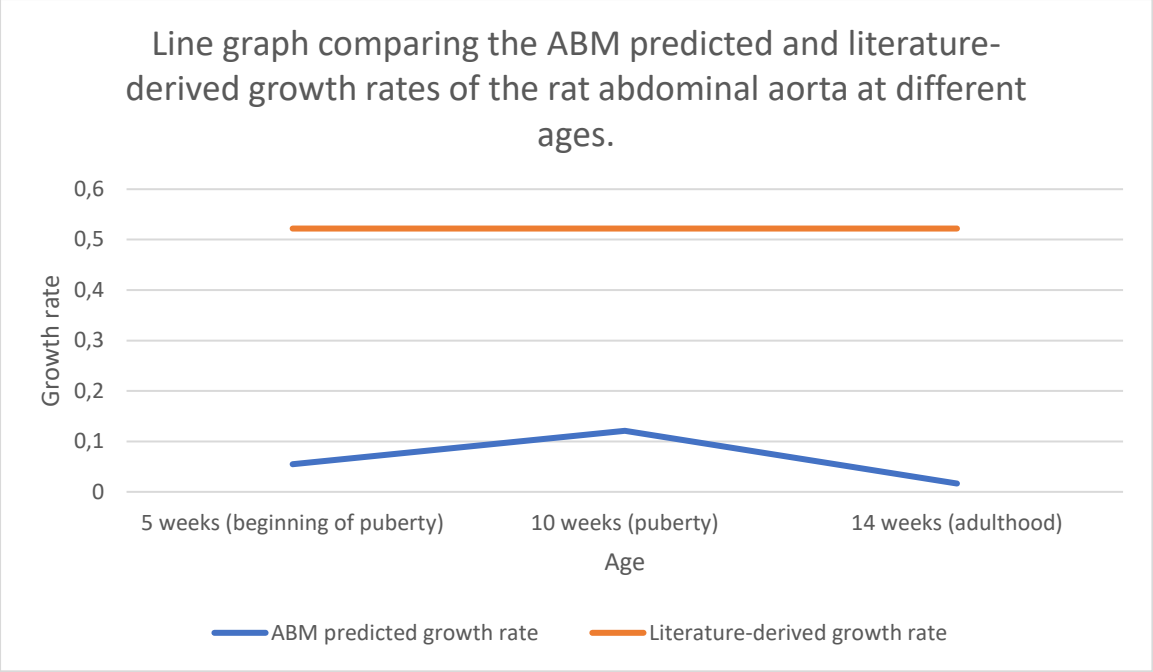

4.1.2 Porcine Carotid Artery

A similar study to the rat abdominal aorta growth ABM was made for the Porcine carotid artery. Growth was simulated and the amount of growth noted at different ages to be compared with literature derived experimental study data. Porcine have a much longer lifespan, therefore a 200 day / ~ 6.5-month period (800 ticks) was simulated. Figure 4.2 (a) shows the growth curve determined by BSA while Figure 4.2 (b) shows the ABM output from NetLogo after a simulation of 6.5-month growth in the porcine carotid artery. Table 4.2 below gives a summary of the output radius.

Table 4.2: Table summary of the output ABM predicted radius for the porcine carotid artery after growth.

Age	**Literature Derived Expected Radius** (cm)	**ABM simulation 1** (cm)	**ABM Simulation 2** (cm)	**ABM Simulation 3** (cm)	**ABM Simulation 4 (cm)**	**ABM Simulation 5** (cm)	**ABM Average radius +- SD (cm)**	**% Difference** (%)
100 Days	0.0505 +- 0.00652	0.05257	0.0534	0.0459			0.0530 +- 0.0006	4.95
160 Days	0.0560 +- 0.0117	0.05698	0.0580	0.0567			0.0575 +- 0.0007	2.68
200 Days	0.0600	0.0605	0.0626	0.0616			0.0616 +- 0.0011	2.67

(a) (b)

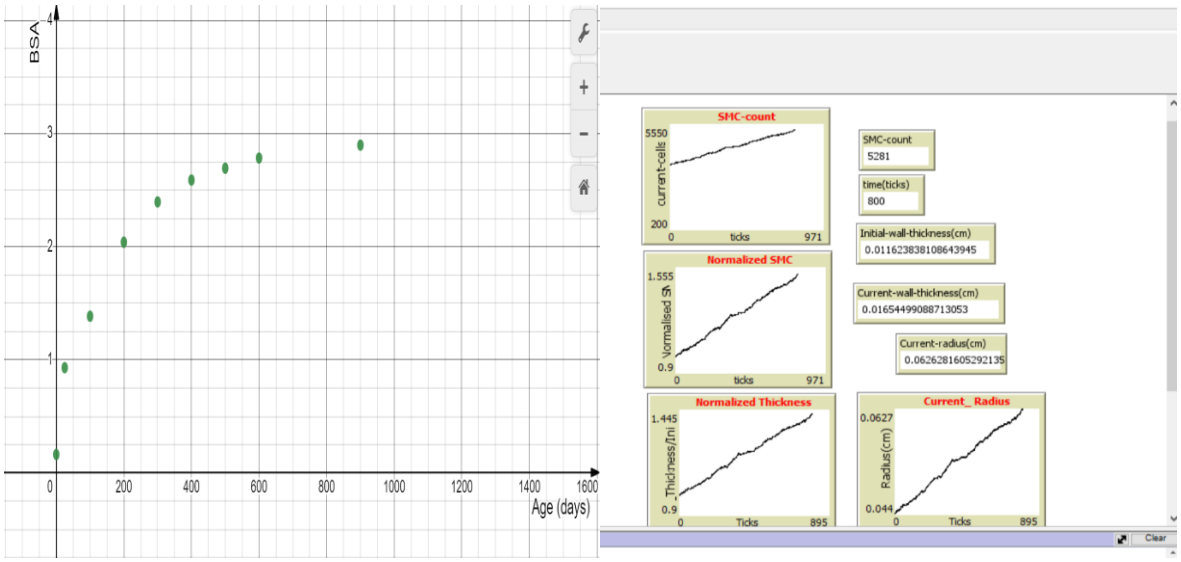

Figure 4.2: (a) Growth curve obtained by considering the BSA against the age of the pig in weeks. (b) A NetLogo simulation output showing the various graphs including the trends of the number of SMCs (SMC-count) against time (in ticks), the normalized number of SMCs against time (in ticks), normalized vessel thickness against time (in ticks) and the luminal radius against time (in ticks). Output windows reflecting the number of SMCs, time (in ticks), initial and current wall thickness, and radius, at any given time are also shown.

Similar to the case in Chapter 4.1.1, Figures 4.2 (a) and (b) were vital in validating the growth ABM for the porcine carotid artery. The growth curve in Figure 4.2 (a) when considering the ages from 35 days to 200 days of maximum growth, had a similar, more linear graph when compared against the ABM simulated vessel thickness and luminal radius predicted growth graphs. In addition, comparing the growth rates showed that the growth rate reduced as the pig aged, thus, supporting the shape of the growth curves in Figure 4.2 (a) and (b). Taking the growth rate over 200 days revealed that the ABM predicted a growth rate of 0.396 while the expected growth rate was 0.360.

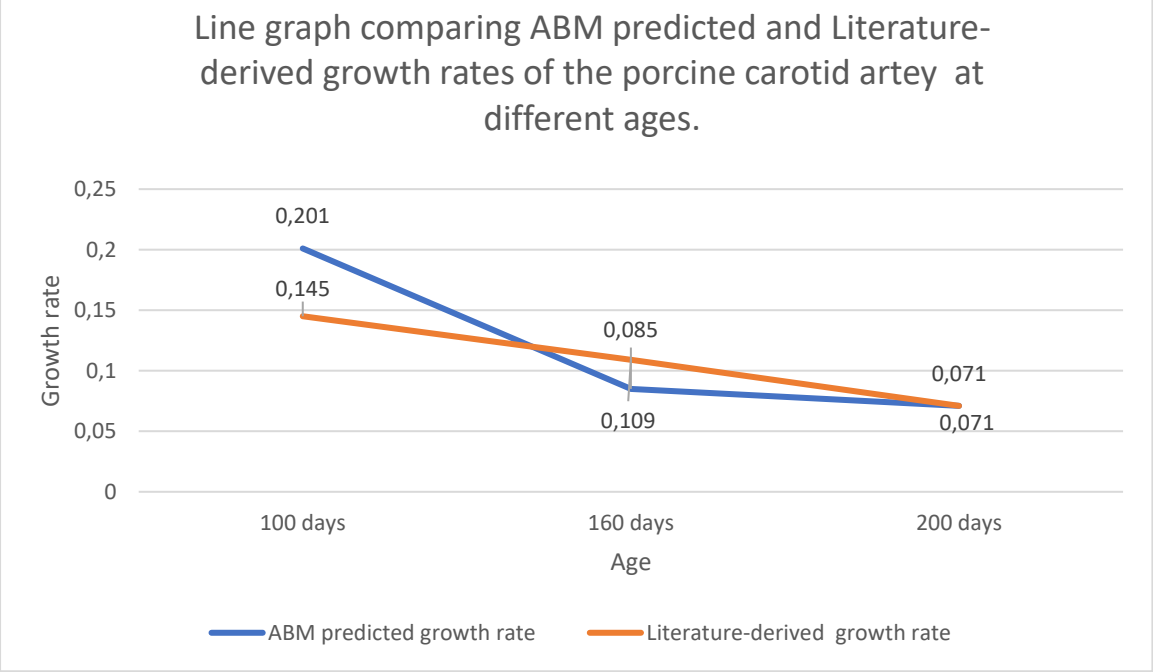

Further validation of the ABM was carried out by studying the ABM predicted growth of the porcine carotid artery luminal radius at different ages and further comparing that with the literature derived experimental study data of the luminal radius of the porcine carotid artery at the specified ages. Table 4.2 clearly shows that the ABM prediction error was less than 5% and got slightly better at its prediction as the pig aged.

4.1.3 Healthy toddler abdominal aorta

The next step-up from the porcine species was the human species. The abdominal aorta of a healthy toddler aged 2.5 years was studied. A literature search produced an experimental study that measured the weight of toddlers every 6 months from age 2 to age 7. This was able to inform an appropriate growth curve shown in Figure 4.3 (a). Another literature search informed the expected luminal radius of the abdominal aorta of a healthy toddler (Table 4.3). NetLogo growth ABM was run to simulate a 6-month period (730 ticks) and growth was captured by the output Table 4.3 and Figure 4.3 (b).

Table 4.3: Table summary of the output ABM predicted radius for the abdominal aorta of a toddler after growth.

Age	Literature Derived Expected Radius (cm)	ABM Simulation 1 (cm)	ABM Simulation 2 (cm)	ABM Simulation 3 (cm)	ABM Simulation 4 (cm)	ABM Simulation 5 (cm)	ABM Average radius +- SD (cm)	% Difference (cm)
3 Years	0.442	0.469	0.490	0.486	0.466	0.483	0.479 +- 0.011	8.4

(a) (b)

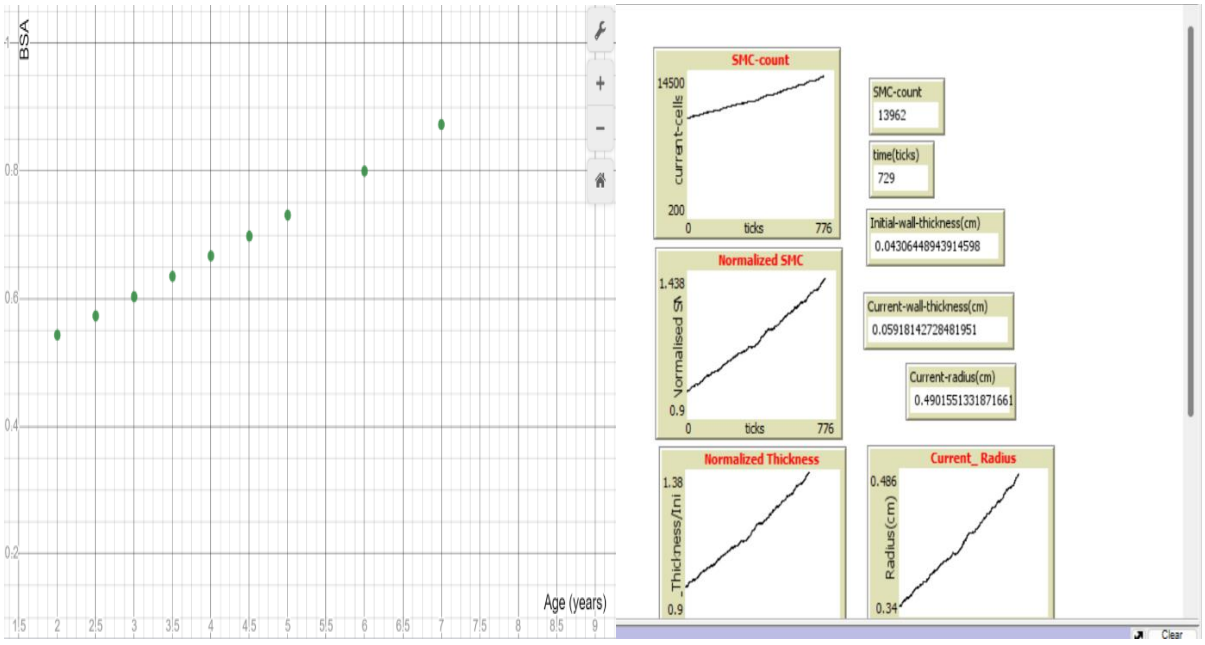

Figure 4.3: (a) Growth curve obtained by considering the BSA against the age of the toddler in years. (b) A NetLogo simulation output showing the various graphs including the trends of the number of SMCs (SMC-count) against time (in ticks), the normalized number of SMCs against time (in ticks), normalized vessel thickness against time (in ticks) and the luminal radius against time (in ticks). Output windows reflecting the number of SMCs, time (in ticks), initial and current wall thickness, and radius, at any given time are also shown.

Figures 4.3 (a) and (b), like Figures 4.1 (a) and (b) and Figures 4.2 (a) and (b) before, serve to validate the growth ABM for the specific vessel. In this case, the ABM prediction thickness and luminal radius growth graphs show a similar linear trend that (the growth curve) expected by the BSA. A more in-depth study of the Table 4.6 shows that the ABM has a prediction error of 8.4% and a growth rate of 0.357.

4.1.4 Patient-specific thoracic aorta

After building up and validating the growth ABM for various species and vessels. The ABM was then tailored to the patient specific thoracic aorta. The patient was aged 18 months and a study was carried out on their unrepaired CoA thoracic aorta. Data was obtained and pre-processed as described in Chapter 3 previously to be used in the ABM (summarised in input Table 3.2). Growth was observed for a 6-month period (730 ticks) at different locations along the thoracic descending aorta and the NetLogo ABM predicted luminal radius after growth for each slice was noted and summarised in Table 4.4.

Table 4.4: Table summary of the output ABM predicted radius for the unrepaired CoA descending aorta of a patient after growth.

Location	**Initial Radius (cm)**	**ABM Simulation 1 (cm)**	**ABM Simulation 2 (cm)**	**ABM Simulation 3 (cm)**	**ABM Simulation 4 (cm)**	**ABM Simulation 5 (cm)**	**ABM Average radius after growth +- SD (cm)**	**Growth rate**
Slice 1 (Before CoA)	0.323	0.483	0.490	0.476	0.471	0.495	0.483 +- 0.010	0.495
Slice 2 (At CoA)	0.155	0.227	0.233	0.227	0.223	0.231	0.228 +- 0.004	0.472
Slice 3 (After CoA)	0.451	0.672	0.658	0.653	0.643	0.653	0.656 +- 0.011	0.454
Slice 4 (After CoA)	0.527	0.771	0.760	0.761			0.764 +- 0.004	0.450

The growth rate was observed for the region around the CoA was similar with an average growth rate of $0.468^{+}_{-}0.010$ and reduced slightly the further down the location of interest was along the length of the descending thoracic aorta.

4.1.5 General observations of the ABM across species

As expected, the ABM simulations were non-deterministic in nature. This was observed by considering the results of the repeat simulations for each set of inputs that varied. Thus, calling for an average of 5 simulations per input-set to be taken.

The growth rates of the vessel thickness and luminal radius in each species reduced as the animal being considered grew over time and this phenomenon was supported by the BSA growth curve derived from literature over time. The prediction error with respect to the growth rate is observed to be 61.3% in rat abdominal aorta (at its worst), 10.0% in porcine carotid artery (at its best) and 35.7% in the healthy toddler's abdominal aorta growth model. The growth rates in the patient specific CoA abdominal aorta were higher than that observed in the healthy toddler's abdominal aorta case. An in-depth study is carried out in Chapter 4.3.1.

Alternatively, the ABM prediction error was less than 30% with respect to the luminal radius. An important observation was that the ABM developed was more accurate at predicting growth in the larger species. The ABM prediction error with respect to the luminal radius was 21.00% in rat abdominal aorta (at its worst), 2.67% in porcine carotid artery (at its best) and 8.40% in the healthy toddler's abdominal aorta growth model.

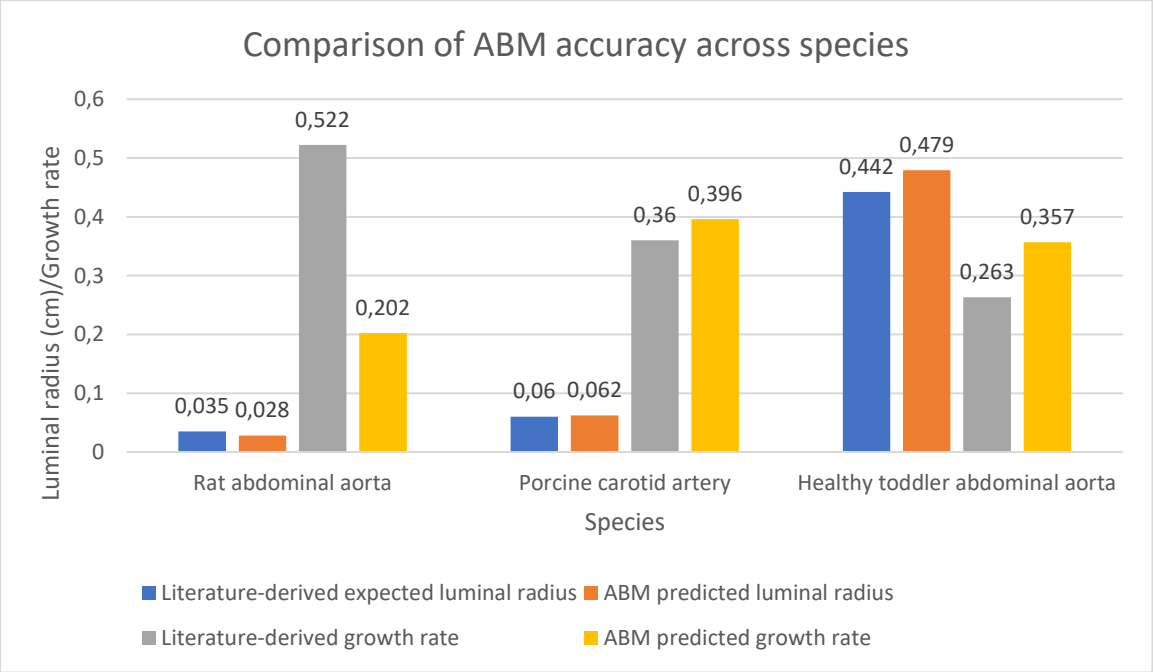

Figure 4.4: Bar graph comparing the ABM accuracy across species.

4.2 Effects of Wall Shear Stress (WSS) and Pressure on growth of the rat abdominal aorta

After the development of the ABM to predict vascular growth, a further study was carried out to investigate the effects of the mechanical stimuli on species specific growth. High blood pressure is characterised by an increase of 30% of its normal blood pressure, therefore, to study the effects of the mechanical stimuli, an increase/decrease by 30% of each stimulus was implemented in the ABM.

4.2.1 WSS

	Change in wall thickness (%)	**Change in luminal radius (%)**
Low WSS	↓1.80	↓5.60
High WSS	↓5.60	↑7.00

Table 4.5: Table summary of the percentage difference in ABM predicted wall thickness and luminal radius with varying WSS from that observed under normal WSS, after a simulated 100 days of growth. High WSS was defined as a 30% increase from normal WSS while low WSS was defined by a reduction of 30% from normal WSS.

The change in WSS had the most effect on the luminal radius with a 30% increase in WSS having a 7% increase in luminal radius. High WSS also is observed to have twice as much impact on the vascular geometry than low WSS.

4.2.2 Circumferential Pressure

	Change in wall thickness (%)	**Change in luminal radius (%)**
Low Circumferential pressure	↓0.70	↓8.50
High Circumferential pressure	↑1.86	↑9.60

Table 4.6: Table summary of the percentage difference in ABM predicted wall thickness and luminal radius with varying circumferential pressure from that observed under normal circumferential pressure, after a simulated 100 days of growth. High circumferential pressure was defined as a 30% increase from normal circumferential pressure while low circumferential pressure was defined by a reduction of 30% from normal circumferential pressure.

Circumferential pressure had the most effect on luminal radius with an 8.50% reduction in radius under low circumferential pressure and a 9.60% increase in radius under a high circumferential pressure. Unlike in the case of varying WSS, low circumferential pressure had approximately as much impact on the vascular geometry as high circumferential pressure.

WSS is observed to have almost 3 times more of an effect on the vessel wall thickness than the circumferential pressure.

4.3 Patient- specific ABM

4.3.1 Healthy toddler vs. Patient-specific case

Vessel	Radius (cm)	WSS (Pa)	Circumferential pressure (KPa)	Growth rate
Before CoA thoracic Slice 1	0.323	3.191	109.978	0.495
At CoA thoracic Slice 2	0.155	58.550	100.443	0.472
After CoA thoracic Slice 3	0.451	2.369	103.970	0.454
After CoA thoracic Slice 4	0.527	2.164	121.773	0.450
Healthy abdominal aorta	0.350	7.420	83.023	0.357

Table 4.7: Table summary comparing the input parameters and ABM predicted average growth rates after a simulated 6-months of growth of the healthy toddler's abdominal aorta against the patient specific unrepaired CoA thoracic aorta.

The portion of the aorta being compared is different in the patient (i.e. descending thoracic aorta) from that in the healthy toddler (i.e. abdominal aorta). The descending thoracic aorta is closer to the heart and blood flow proceeds into the abdominal aorta from the thoracic aorta. As can be noted the pressure experienced in the thoracic aorta is higher and gradually reduces down the aorta. The patient's thoracic aorta is observed to have a higher ABM predicted average growth rate of 0.468 while the healthy abdominal aorta predicted average growth rate is 0.357. The growth rates follow the same trend as the circumferential pressure, reducing the further down along the aorta where the location of observation is.

In the patient, the smallest radius, about 57.8% smaller than the other points of study, is at the point of CoA and that point experiences the highest WSS, almost 20 times that experienced at locations before and after the CoA. Slice 1 has a radius 0.716 times that of slice 3, however, it experiences a WSS 34.7% higher than Slice 3. Slice 1 in the patient has a radius similar to the healthy toddler, however, the WSS is about twice as high in the healthy toddler than in the patient's slice 1. Furthermore, WSS in slice 3 is about 3 times lower than that experienced in the abdominal aorta, where the radius is only 0.1cm larger in the patient's slice 3 than the healthy abdominal aorta.

4.3.2 Pre-growth vs Post-growth

An in-depth analytical study was carried out for the patient-specific thoracic aorta before and after the ABM growth prediction.

(a) Luminal radius

Growth has been defined as the change in luminal radius in this study. Therefore, the analysis of the radial changes at the locations of observation i.e. Slice 1 (before CoA), Slice 2 (at CoA), Slice 3 (after CoA) and Slice 4 (after CoA) is considered.

As can be noted from Figure 4.5, there is an increase in radius at each location. The smallest radial change is observed at the coarctation point (Slice 2) with an increase in radius of 0.73mm compared to 1.60mm, 2.05mm and 2.37mm changes in radius observed at the locations before (Slice 1) and after (Slice 3 and Slice 4) the coarctation point, respectively. However, it was observed that the growth rates at these locations reduce the further down the location of observation is along the length of the thoracic aorta. The growth rate was highest at Slice 1 with a rate of 0.4954, 0.4723 at Slice 2, 0.4541 at Slice 3 and a rate of 0.4497 at Slice 4.

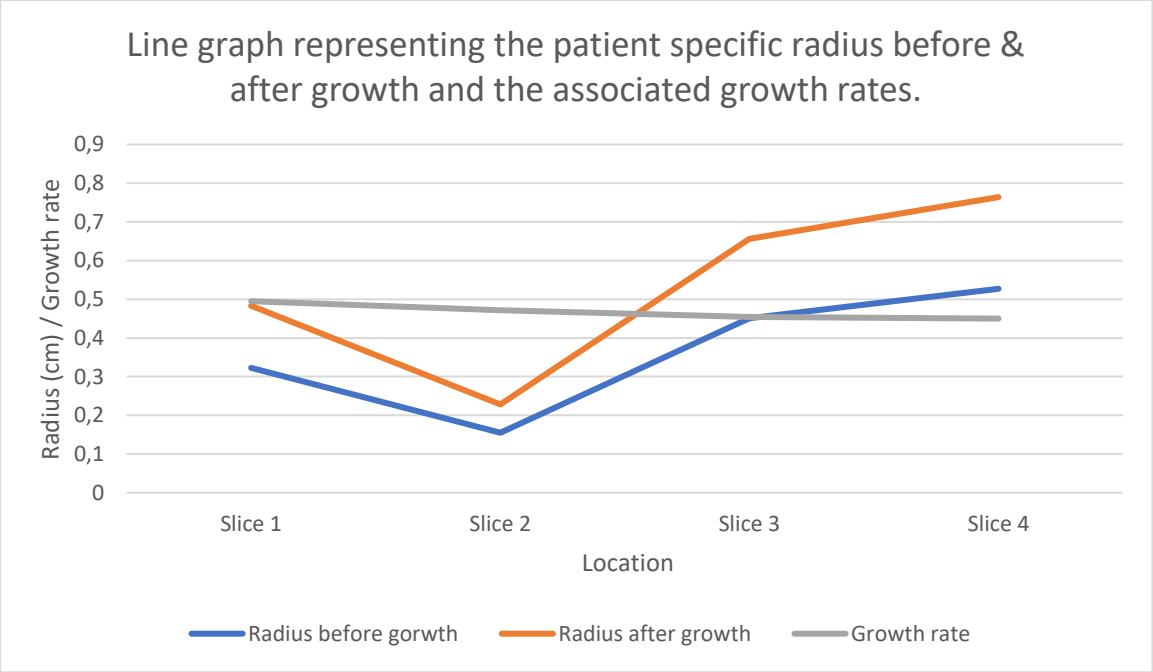

Figure 4.5: Line graph representing the ABM-predicted evolution of the patient-specific thoracic aorta luminal radius at 4 locations; Slice 1 (before CoA), Slice 2 (at CoA), Slice 3 (after CoA) and Slice 4 (after CoA), with their associated growth rates.

(b) WSS

In a similar way, the WSS analysis pre-growth and post-growth is considered.

The line graph depicts the WSS distribution before and after growth at the aforementioned 4 locations.

It is observed from Figure 4.6 that the WSS spikes at the point of CoA (Slice 2) both before and after growth. In addition, there is a reduction in WSS after growth in Slices 1, 2 and 3, while an increase in WSS is observed Slice 4. The greatest change in WSS of -20.2114

Pa is observed at the point of CoA; however, the largest percentage change is observed at Slice 4, experiencing a 140.52% increase in WSS. Slice 2 experiences a 34.52% decrease in WSS, while Slices 1 and 3 experience 12.39% decrease in WSS and 11.83% decrease in WSS respectively.

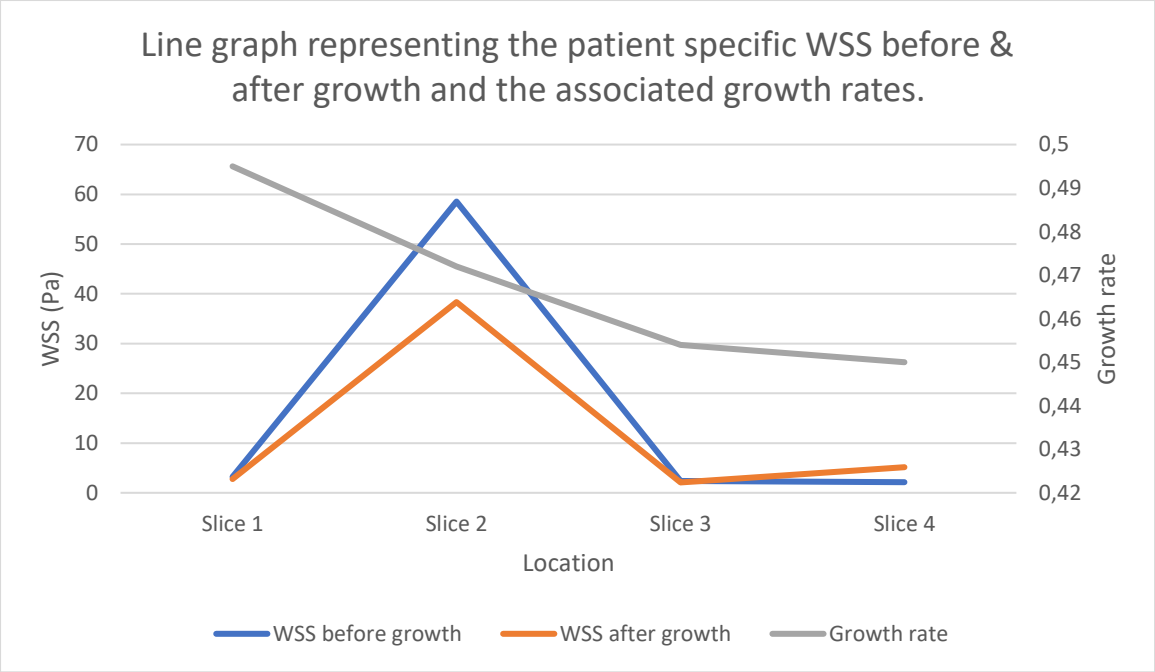

Figure 4.6: Line graph representing the evolution of the patient-specific thoracic aorta WSS before and after ABM-predicted growth at 4 locations; Slice 1 (before CoA), Slice 2 (at CoA), Slice 3 (after CoA) and Slice 4 (after CoA), with their associated ABM growth rates.

This trend is further corroborated by the output CFD Figure 4.7 below depicting the WSS distribution before and after growth. The WSS is highest at the CoA region both before and after growth. Further observations show that the turbulent blood flow jet shoots out further down the thoracic aorta after growth, slightly reducing the concentration in the previous turbulent region but increasing it below the initial turbulent region.

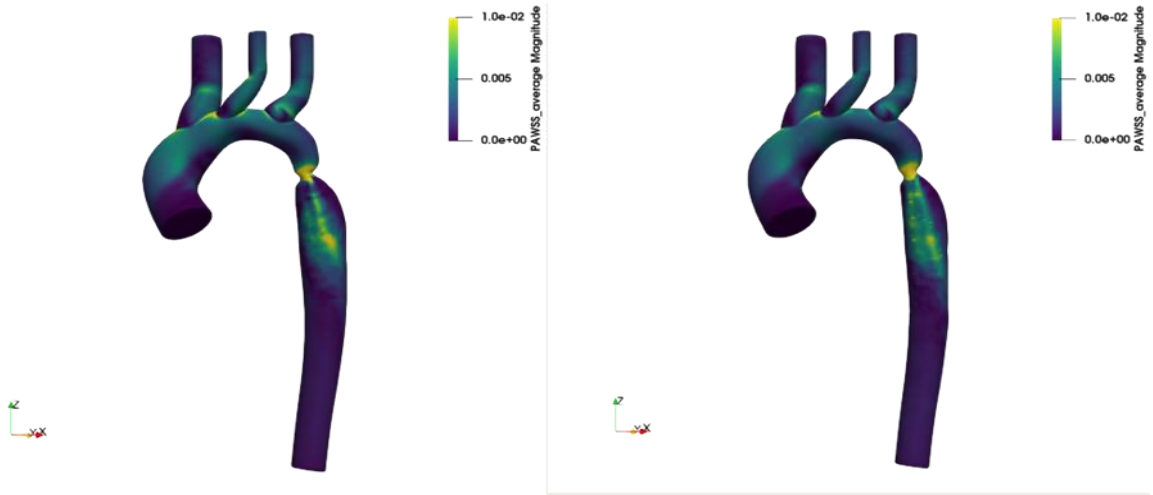

Figure 4.7: Visual depiction of patient-specific wall shear stress distribution before ABM predicted aortic growth (left) and after ABM predicted aortic growth over 6 months (right).

(c) Pressure

A further study was carried out to consider the effects of growth on the pressure. Two forms of the pressure are considered:

i. Blood pressure obtained directly from the CFD haemodynamic flow profile. It gives rise to forces that drive growth.
ii. Circumferential pressure arising from the blood pressure. It has been previously determined that this pressure drives growth directly and has been captured in the ABM.

The line graphs in Figure 4.8 and Figure 4.9 depict the evolution of the blood pressure and circumferential pressure before and after the ABM predicted growth at 4 locations along the patient-specific thoracic aorta.

Figure 4.8 shows an increase in blood pressure after growth. Slice 4 experiences a 1.03% change in blood pressure whereas Slices 1, 2 and 3 experience 14.18%, 16.09% and 16.53%. There is noticeably minimal change in the blood pressure at Slice 4 which is further away from the region of CoA, compared to Slices 1, 2 and 3 that are within the region of CoA.

Similarly, Figure 4.9 shows that the circumferential pressure increases after growth in the aorta except at Slice 4. The circumferential pressure at Slice 4 decreases by 6.97%. Unlike the blood pressure change pattern, there is more variation in the rest of the locations of observation. Slice 2 has the highest change in circumferential pressure with a 22.09% increase, Slice 1 with a 13.80% increase and Slice 3 with a 6.72% increase.

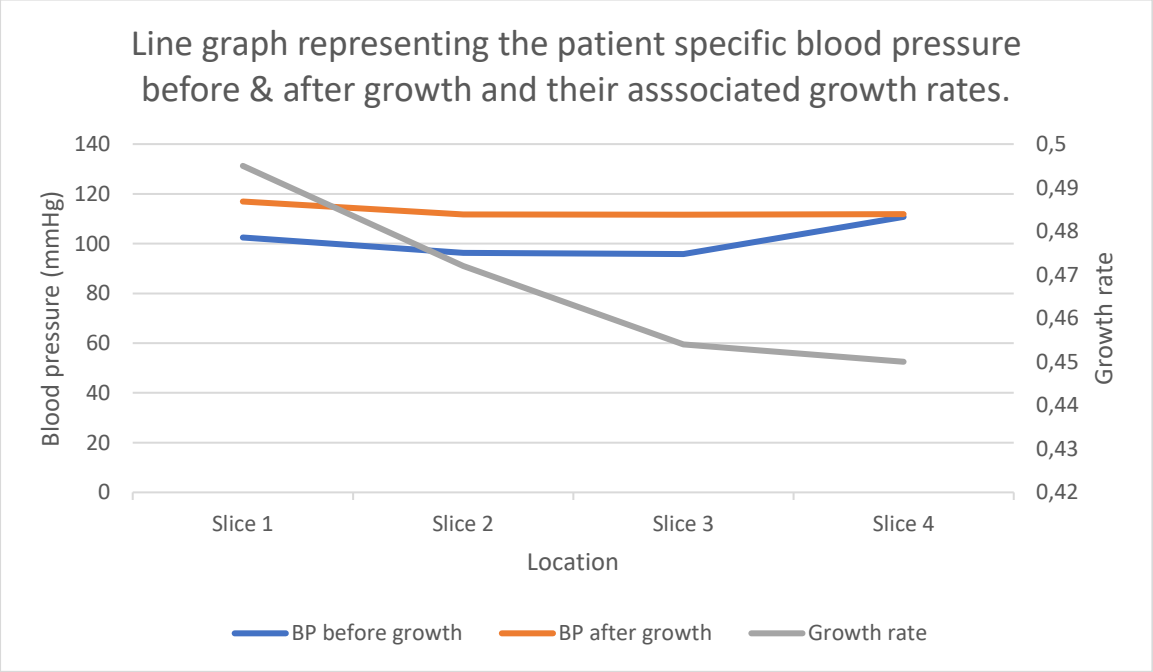

Figure 4.8: Line graph representing the evolution of the patient-specific thoracic aorta blood pressure before and after ABM-predicted growth at 4 locations; Slice 1 (before CoA), Slice 2 (at CoA), Slice 3 (after CoA) and Slice 4 (after CoA), with their associated growth rates.

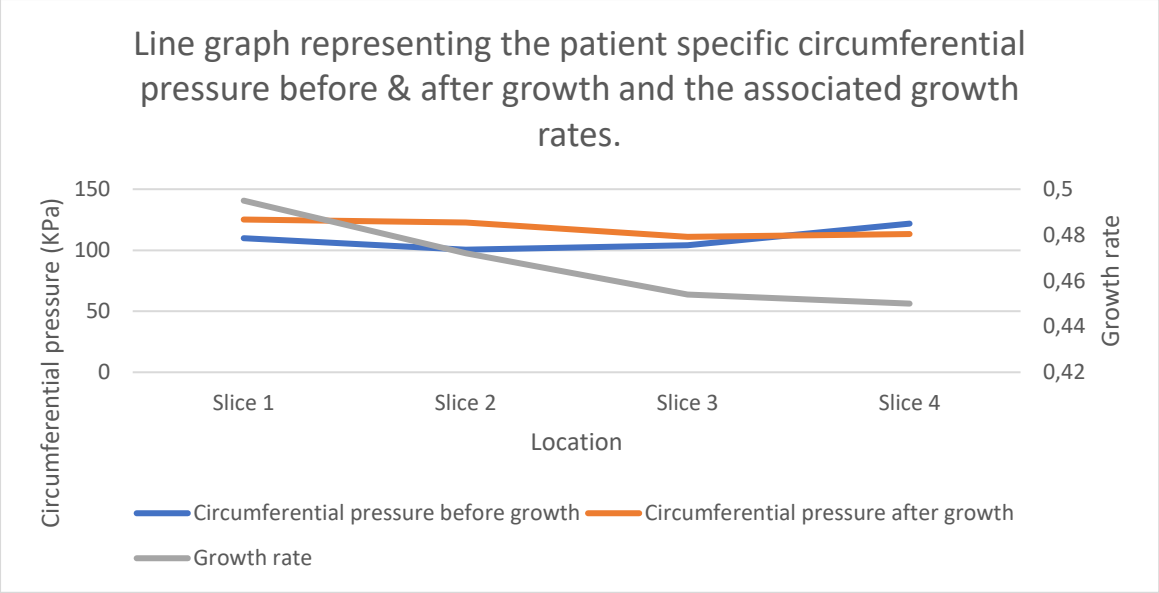

Figure 4.9: Line graph representing the evolution of the patient-specific thoracic aorta circumferential pressure before and after ABM-predicted growth at 4 locations; Slice 1 (before CoA), Slice 2 (at CoA), Slice 3 (after CoA) and Slice 4 (after CoA), with their associated growth rates.

The CFD output Figure 4.10 depicting the blood pressure distribution shows that the blood pressure in the patient-specific descending thoracic aorta is highest before the CoA region, reduces as blood flows through the CoA region and further drops below the CoA region. Another observation of note is the slight increase in the blood pressure in the region after the CoA.

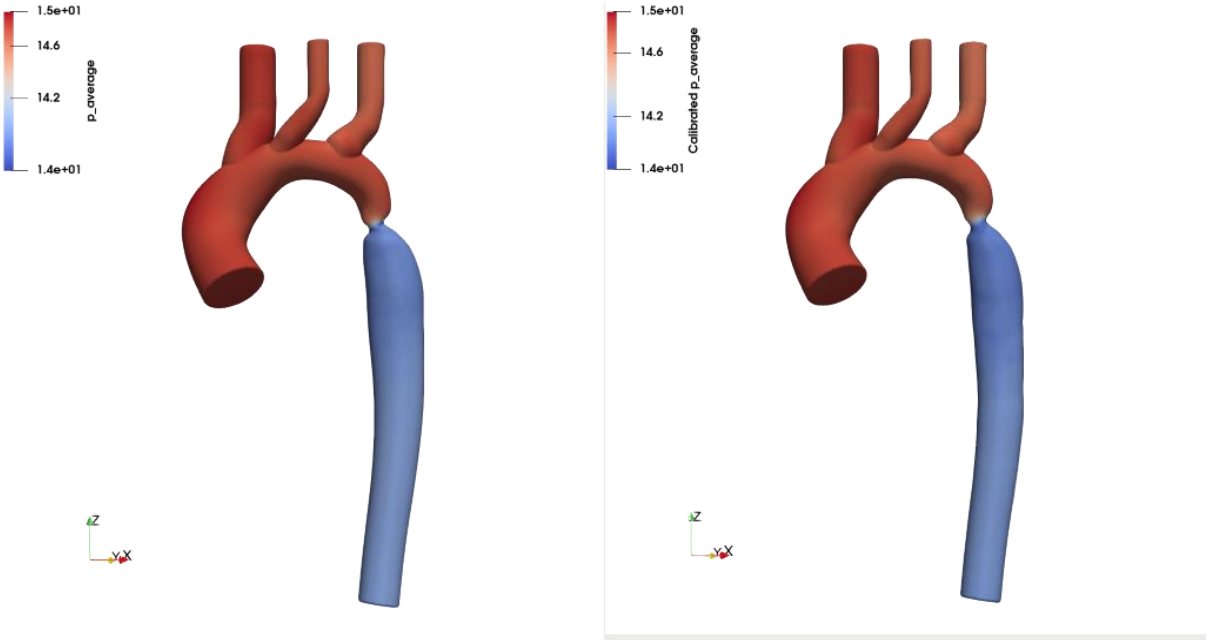

Figure 4.10: Visual depiction of patient-specific blood pressure distribution before ABM predicted aortic growth (left) and after ABM predicted aortic growth over 6 months (right).

Industry standards for good model accuracy is above 70% [75]. Anything more than 70% is considered a useful and acceptable model data output [76]. The ABM developed for the rat abdominal aorta performed well with an accuracy of 79%, with respect to the luminal radius prediction, but poorly when the growth rate was considered, with an accuracy of 39%.
However, this ABM served well in the verification and validation process of being able to reflect the growth of the rat throughout life, due to its short lifespan. The growth curves of juvenile animals are typically sigmoid, implying that while growth is essentially exponential at first, it slows down to almost zero as the animal gets closer to maturity [77]. This phenomenon has been captured mathematically by the Von Bertalanffy [78], Logistic [79] and Gompertz [80] growth models. Growth in an individual is understood to occur when proliferation rate is higher than the apoptosis rate of the cells. In animals, a growth spurt is observed during puberty until the individual reaches its mature/adult body. At different stages in life, various processes are prioritized over others. More resources are allocated to growing cells, during puberty but as the individual increases in size, the resources are then diverted to maintaining the mature cells [78]. This growth leads to an increase in the BSA, which in turn, is correlated with the aortic diameter [53][54]. The ABM was able to capture the sigmoidal growth curve and correctly determine the growth rate increasing to its peak during puberty and then reducing as it approached adulthood.

The ABM was observed to perform much better in the larger species. In the porcine carotid artery, the ABM had a prediction accuracy of between 95.05% and 97.33% with respect to the luminal radius output variable, and 90% with respect to the growth rate. Since the porcine genome, size and anatomy are closer to the human than the rodent [51], this validation step provided the confidence required to adapt the ABM to the healthy toddler case.

Similarly in the healthy toddler abdominal aorta, its ABM prediction accuracy with regards to the luminal radius was 91.6% but performed poorly in its growth rate prediction with 64.3% accuracy. However, a literature search revealed that: at age 2.5 a healthy toddler on average weighs 28 lb 11 oz (13 kg) and has an average height of 2 ft 11.5 in (90.3 cm) [57]. During the third year of life, most toddlers gain about 4 pounds (1.8 kg) and grow about 2 to 3 inches (5 to 8 cm) [58]. Given this data, the BSA derived growth rate from age 2.5 years to 3 years old of a healthy toddler is 0.357. Comparing this against the ABM predicted growth rate of the healthy toddler abdominal aorta, it is observed that the growth rate is the same. This is a good validation step in the model development and provides further confidence to adapt the ABM to the patient-specific case.

The ABM rules and input variables were obtained from a literature search of experimental research. However, a consistent, comparable, and complete set of data could not be created for an individual species, as well as the same vessel across species. In addition, the method of experimentation was not consistent. A collection of ABM rules from various sources was created ranging from experiments carried out in aortic smooth muscle cells in juvenile [67] and adult [68] Sprague Dawley rats [67], to aortic bovine endothelial cells [72][74] and human umbilical vein endothelial cells [73].
The assumption to keep the rule-set constant and adjust the species-specific input variables of vascular thickness and luminal radius, was supported by the good ABM prediction accuracy in all three species, that is, except the growth rate prediction for the rat abdominal aorta.

According to the ABM solver environment, the species-specific variation in thickness represented a proportional variation in the number of agents. Hence, the simulation time increased as the species under observation got larger, although the ABM observation time of 6 months of growth in nature in each study remained constant (except in the case of the rat abdominal aorta). Thus, the simulation time is dependent on the number of agents in the system. This can be explained by the fact that the ABM allows for each agent interaction with itself, and with other agents and its environment. More

agents (cells) allow for more possible interactions during the simulation. The table 5.1 shows a breakdown of each species and its simulation time.

Species and vessel	Number of cells (or agents)	Observation time	ABM Simulation time
Rat abdominal aorta	472	3.5 months	< 5min
Porcine carotid artery	3638	6 months	~ 4 hours
Healthy toddler abdominal aorta	10053	6 months	~ 24 hours
Patient thoracic aorta	2053 - 22453	6 months	~ 3 – 26 hours

Table 5.1: A breakdown of the simulation time for each species.

The principle of repetition maintains stability in both the mean and standard deviation, enabling sample statistics to accurately reflect the characteristics of the population. As a result, the statistical inference can be trusted [81]. When assessing the distribution of the data, three repeats are typically a decent place to start [82]. Compared to the traditional CMM growth model, the ABM is non-deterministic by design, therefore, the application of having 3 to 5 repeat simulations was supported. Its non-deterministic nature was reflected by variations in predicted output for each repeat, therefore, being able to mirror the non-deterministic nature of biological organisms.
Although it is not well suited for capturing the fundamental molecular and cellular level mechano-bio-chemical reactions, continuum biomechanics is well suited to relate measurable blood pressures and flows to the stresses and strains in the artery wall in a way that frequently corresponds well with pathogenesis and disease progression [22]. CMM, first proposed by Humphery and Rajagopal [83] is a continuum representation of the mechanobiology of growth. Several studies have shown that CMM is stable against transient reasonable perturbations of pressure [22]. In the comparative study by Hayenga [22], both the CMM and ABM did not experience growth when pressure was increased by 30% for 1-tick (representing 6-hours in nature). Therefore, in the ABM development, growth is only expected under sustained change in pressure or an unreasonable transient change in pressure. A further CMM and ABM comparative study of hypertension [22], resulted in the output variables being very similar. However, the ABM, due to its nature, was not able to directly output the luminal diameter changes. This led to the assumption that the change in vessel wall thickness was proportional to the change in luminal diameter. This literature comparative study supported the adoption of the ABM, a discrete growth model, which is better suited to incorporate Aim 2 (genetic expression of growth factors and hormones) of the PROTEA project into Aim 3 (computational modelling of growth).

The growth rate of the healthy toddler abdominal aorta provides us with the baseline growth pattern of the toddler. The patient-specific growth rate is observed to be generally higher than that of the healthy toddler. This shows that the geometry of the vessel affects the haemodynamic patterns i.e., mechanical stimuli, in turn affecting the growth. It is of interest that the growth rate in the diseased case is similar at the 4 observation points (Slices 1 ,2, 3 and 4), averaging a rate of 0.468. Conversely, the change in radius is smallest at the point of CoA, this suggests that the CoA will not resolve on its own as the patient ages.

The blood pressure observed in the patient-specific case is generally higher than the blood pressure in a healthy toddler (an average of systolic and diastolic blood pressure at 76.5 mmHg). This is characteristic of this condition given that the heart must work harder to push blood through the CoA. However, the blood pressure had not crossed the threshold of 105 mmHg [59] to be considered high blood pressure in a child. After the ABM predicted growth, the blood pressure is observed to increase to and moves towards a more constant blood pressure throughout the vessel. This is a phenomenon known as homeostasis. However, in this diseased case, the constant blood pressure approached is higher than that expected in a healthy child at that age, therefore, the blood pressure approaches an

adaptive homeostatic state [60]. At age 3, the patient is thus predicted to suffer from High blood pressure.

The circumferential pressure obtained from blood pressure is understood to be one of the mechanical stresses that directly contribute to growth. This circumferential pressure acting on the aortic wall cells (dependent on their distance from the lumen), by the process of mechanotransduction, produced a PDGF-AB concentration profile which is proportional to the proliferation rate of the SMC (refer to Table 3.1). This then directly determined the vascular wall thickness due to increased SMC mass, thus growth. The circumferential pressure pattern thus varies more than the blood pressure as it is proportional to not only the blood pressure but also the thickness of each slice. The circumferential pressure is then understandably highest at the CoA and lowest in the region further along after the CoA.

The blood pressure pattern created by the CoA leads to the creation of a steeper pressure gradient than is experienced by the aortic structure in the healthy toddler case. This leads to the build-up of turbulent flow past the CoA region, hence increasing the general WSS in this region, and more specifically, the WSS distribution varies a lot more in the region. This is observed in the pre vs post CFD shots in Figure 4.7. Furthermore, the WSS distribution after growth shows a larger region of increased WSS below the CoA.

Like the circumferential pressure, the WSS, by the process of mechanotransduction experienced by the Endothelial cells, produces the growth hormone in a piecewise function as is described in the ABM rule is Table 3.1. The growth hormone then provides an environment for the growth factor PDGF-AB concentration profile to be created, directly contributing to the proliferation rate, thus leading to the growth of the vessel. In this study, the magnitude of WSS is good enough to predict growth, as it was small. The need to have WSS represented as a vector at each discrete point along the 2D vascular wall arises when the WSS is higher in order to predict growth more accurately. According to the piecewise function (refer to Table 3.1), its contribution becomes more complex. In addition, when WSS goes above a particular threshold, possible damage to the wall should be allowed for, thus remodelling of the vessel wall should be considered in the model development. Hence, a more accurate simulation of the patient-specific case as the child ages would call for remodelling to be considered in the ABM development. The vessels in the validation species- specific cases are assumed to be of the structure similar to a uniform pipe, hence a 2D cross section disc is a good representation of the 3D vascular structure. However, in the patient specific case, the vessel has a more complex structure owing to the nature of the patient's condition. This is more suitably represented by various cross section 2D slices taken along of the 3D patient vessel. A representative disc in each region of the patient's aorta was taken (before the CoA, at CoA, and 2 after CoA) to have a more accurate and continuous study of the 3D vessel. The growth of each slice is studied separately in the ABM. These ABM predicted 2D grown structures are integrated and smoothed into a 3D structure using interpolation, and the haemodynamic flow is studied in this patient-specific predicted 3D vessel.

Chapter 5: CONCLUSION & RECOMMENDATIONS

In summary, an understanding of the complex mechano-chemo-biological mechanism involved in aortic growth in an ABM was grasped through the literature review exercised in Chapter 2.

Consequently, a simplistic but comprehensive list of key contributors to growth was established in Chapter 3.4. The blood flow components of circumferential pressure and wall shear stress were defined as the input mechanical variables that drive growth and their effects on growth were captured in the ABM through the list of rules, describing the complex mechanobiochemical processes, including PDGF-β, TGF-AB, NO and smooth muscle cell proliferation and apoptosis rates. This mechanotransduction process was implemented into NetLogo by a set of mathematical formulations reflecting the rules. This study was therefore able to develop an ABM to partially satisfy Aim 3 (by computationally modelling growth) of the PROTEA project and incorporate Aim 2 (genetic expression of growth factors and hormones).
The assumptions made to exclude the elastin and collagen turnover were valid as they are known to directly affect remodelling, and not growth. However, in the patient-specific case, a pathology is present and thus, the material properties of the vascular wall might very well be different and changing. Therefore, the ABM would have to incorporate the elastin and collagen turnover in its rules to model this diseased case more accurately.

Chapter 3.4 went on to describe the implementation of the ABM solver to generate suitable results i.e. change in vascular wall thickness and its associated change in luminal radius. These results were then used to determine growth through ABM post-processing and statistical tools described in Chapter 3.5 and Chapter 3.6, respectively, by calculating the growth rate.

Using the predicted luminal radial change and growth rate, the vascular geometry was updated in the CFD, and a haemodynamic study run in the new (grown) geometry. At age 3, the ABM predicted that the patient's CoA would not resolve with age (growth), and they were predicted to develop hypertension. The patient was also predicted to be at risk of injury to the aorta due to the development of turbulent flow after growth, thus putting them at risk of thrombosis development.

In the patient-specific case a coupled model was created by the collaborative work of *Jie Wang* to capture the mechanical stresses of the blood flow through CFD, and this study, to capture the biochemical processes leading to growth using the ABM. This manual coupling (laid out in Chapters 3.2 and 3.3) was successful in observing the effects of growth on haemodynamic flow patterns. However, this manual coupling is tedious and cumbersome. Creating a direct computational link between the CFD and ABM would be more effective allowing for more slices to be studied for each growth iteration, making the coupled growth model more accurate. It would also allow for more growth iterations to be studied to make the coupled growth model more effective.

The comparative medicine approach proved beneficial to this study. The rat, porcine and healthy toddler growth models served as good verification of concept and validation steps during the model development process. The ABM performed much better in the larger animals, with prediction accuracies of above 90%. This species-specific validation step provided the confidence to adapt the ABM to the patient-specific case.

Bibliography

[1] C. A.Warnes et al., aACC/AHA 2008 Guidelines for the Management of Adults with Congenital Heart Disease: a report of the American College of Cardiology/American Heart Association Task Force on Practice Guidelines (writing committee to develop guidelines on the management of a,a Circulation, vol. 118, no. 23, pp. 765a768. (2008).

[2] Congenital Heart Defects - Facts about Coarctation of the Aorta | CDC. (2019) Available from: https://www.cdc.gov/ncbddd/heartdefects/coarctationofaorta.html

[3] Cleveland Clinic. (2019) Available from: https://my.clevelandclinic.org/health/diseases/16876-aortic-coarctation

[4] AskMayoExpert. Coarctation of the aorta: Signs and symptoms. Rochester, Minn.: Mayo Foundation for Medical Education and Research. (2017).

[5] Johns Hopkins Medicine. (2020) Available from: https://www.hopkinsmedicine.org/health/treatment-tests-and-therapies/pulseoximetry

[6] E.G.M. Hoosen, A.M. Cilliers, C.T. Hugo-Hamman, S.C. Brown, J.B.Lawrenson, L. Zuhlke, et al . Paediatric cardiac services in South Africa. SAMJ, S. Afr. med. j. [Internet]. 101(2): 106-106. Available from: http://www.scielo.org.za/scielo.php?script=sciarttext&pid=S0256-95742011000200017&lng=en. (2011)

[7] D. Sagan, C. Sagan, L. Margulis and R. Shiri. EncyclopA|dia Britannica, inc. (2020). Available from: https://www.britannica.com/science/life

[8] A.Goriely. The Mathematics and Mechanics of Biological Growth. Springer. (2017)

[9] M. Eskandari and E. Kuhl. Systems biology and mechanics of growth. (2015) Available from: WIREs Syst Biol Med 2015, 7:401a412. doi: 10.1002/wsbm.1312

[10] D. Ambrosi,MBen-Amar, C.J. Cyron , A. DeSimone, A. Goriely, J.D. Humphrey, E. Kuhl. Growth and remodelling of living tissues: perspectives, challenges and opportunities. J. R. Soc. (2019). Interface 16: 20190233. Available from: http://dx.doi.org/10.1098/rsif.2019.0233

[11] J.S. Huxley. Problems of Relative Growth. pp 1-68. Methuen &Co. Ltd. (1935)

[12] L.C. Lee, G.S. Kassab, and J.M. Guccione. Mathematical Modeling of Cardiac Growth and Remodeling. Wiley Interdiscip Rev Syst Biol Med . ; 8(3): 211a226. doi:10.1002/wsbm.1330 (2016)

[13] K.Y.. Volokh.Stresses in growing soft tissues. Department of mechanical engineering, Johns HopkinsUniversity, Baltimore. (2006)

[14] Soft tissue injuries|Sports Medicine Australia. (2020) Available from: https://sma.org.au/resources-advice/injury-fact-sheets/soft-tissue-injuries/

[15] M. A. Quetelet. A treatise on man and the development of his faculties.William and Robert Chambers. 1835

[16] T. Arts, F.W. Prinzen, L.H.E.H Snoeckx , J.M. Rijcken, R.S. Reneman. Adaption of cardiac structure by mechanical feedback in the environment of the cell: A model study. Biophys. J.; 66(4):953a 961. [PubMed: 8038399] (1994)

[17] J.D. Humphrey Finite Elasticity. In: Cardiovascular Solid Mechanics. Springer, New York. (2002)

[18] D. Ambrosi, G. A. Ateshian, E. M. Arruda, S. C. Cowin, J. Dumais, A. Goriely, G. A. Holzapfel, J. D. Humphrey, R. Kemkemer, E. Kuhl, J. E. Olberding, L. A. Taber, and K. Garikipati. Perspectives on biological growth and remodeling. J Mech Phys Solids. 59(4): 863a883. doi:10.1016/j.jmps.2010.12.011 (2011)

[19] E. Kuhl, R. Maas, G. Himpel and A. Menzel. Computational modeling of arterial wall growth Attempts towards patient specic simulations based on computer tomography. Springer (2006).

[20] R. Vandiver and A. Goriely. Differential growth and residual stress in cylindrical elastic structures. Phil. Trans. R. Soc. A (2009)

[21] B. C. Thorne, A. M. Bailey and S. M. Peirce. Combining experiments with multi-cell agent-based modeling to study biological tissue patterning. Briefings in Bioinformatics. VOL 8. NO 4. pp 245-257(2007).
Available at: https://academic.oup.com/bib/article/8/4/245/221203

[22] H. N. Hayenga. Mechanics of Atherosclerosis, Hypertension Induced Growth, and Arterial Remodeling. Submitted to the Office of Graduate Studies of Texas AM University in partial fulfillment of the requirements for the degree of DOCTOR OF PHILOSOPHY. (2011)
Available at: https://oaktrust.library.tamu.edu/handle/1969.1/ETD-TAMU-2011-05-90986

[23] B. C. Thorne, H. N. Hayenga, J. D. Humphrey and S. M. Peirce. Toward a multi-scale computational model of arterial adaptation in hypertension: verification of a multi-cell agent based model. Frontiers in Physiology. VOL 2. ARTICLE 20. (2011).
Available at: https://www.frontiersin.org/articles/10.3389/fphys.2011.00020/full

[24] M. Keshavarzian, C. A. Meyer, and H. N. Hayenga. Mechanobiological model of arterial growth and remodeling. Biomech Model Mechanobiol. 17(1): 87–101. doi:10.1007/s10237-017-0946-y (2018)

[25] A. Corti, M. Colombo, F. Migliavacca, J. F. R. Matas, S. Casarin and C. Chiastra. Multiscale Computational Modeling of Vascular Adaptation: A Systems Biology Approach Using Agent-Based Models. Front. Bioeng. Biotechnol. 9:744560. doi: 10.3389/fbioe.2021.744560 (2021)

[26] J. Walpole, J. A. Papin and S. M. Peirce. Multiscale Computational Models of Complex Biological Systems. Annu. Rev. Biomed. Eng. 15, 137–154. doi:10.1146/annurev-bioeng-071811-150104 (2013)

[27] E. Bonabeau. Agent-based Modeling: Methods and Techniques for Simulating Human Systems. Proc. Natl. Acad. Sci. 99, 7280–7287. doi:10.1073/pnas.082080899 (2002)

[28] G. An, Q. Mi, J. Dutta-Moscato, and Y. Vodovotz. Agent-based Models in Translational Systems Biology. Wires Syst. Biol. Med. 1, 159–171. doi:10.1002/wsbm.45 (2009)

[29] R. Bhui and H. N. Hayenga. An Agent-Based Model of Leukocyte Transendothelial Migration during Atherogenesis. Plos Comput. Biol. 13, e1005523–23. doi:10.1371/journal.pcbi.1005523 (2017)

[30] A. Corti, S. Casarin, C. Chiastra, M. Colombo, F. Migliavacca and M. Garbey. "A Multiscale Model of Atherosclerotic Plaque Development: Toward a Coupling between an Agent-Based Model and CFD Simulations," in Lecture Notes in Computer Science (Including Subseries Lecture Notes in Artificial Intelligence and Lecture Notes in Bioinformatics), 410–423. doi:10.1007/978-3-030-22747-0_31 (2019)

[31] A. Corti, C. Chiastra, M. Colombo, M. Garbey, F. Migliavacca and S. Casarin. A Fully Coupled Computational Fluid Dynamics - Agent-Based Model of Atherosclerotic Plaque Development: Multiscale Modeling Framework and Parameter Sensitivity Analysis. Comput. Biol. Med. 118, 103623. doi:10.1016/ j.compbiomed.2020.103623 (2020)

[32] A. Caiazzo, D. Evans, J. L. Falcone, J. Hegewald, E. Lorenz, B. Stahl, et al. A Complex Automata Approach for In-Stent Restenosis: Two-Dimensional Multiscale Modelling and Simulations. J. Comput. Sci. 2, 9–17. doi:10.1016/j.jocs.2010.09.002 (2011)

[33] D. R. Nolan, and C. Lally. An Investigation of Damage Mechanisms in Mechanobiological Models of In-Stent Restenosis. J. Comput. Sci. 24, 132–142. doi:10.1016/j.jocs.2017.04.009 (2018)

[34] P. S. Zun, A. J. Narracott, C. Chiastra, J. Gunn, and A. G. Hoekstra. Location-Specific Comparison between a 3D In-Stent Restenosis Model and Micro-CT and Histology Data from Porcine In Vivo Experiments. Cardiovasc. Eng. Tech. 10, 568–582. doi:10.1007/s13239-019-00431-4 (2019)

[35] M. Garbey, M. Rahman, and S. A. Berceli. A Multiscale Computational Framework to Understand Vascular Adaptation. J. Comput. Sci. 8, 32–47. doi:10.1016/j.jocs.2015.02.002 (2015)

[36] M. Garbey, S. Casarin and S. A. Berceli. A Versatile Hybrid Agent-Based, Particle and Partial Differential Equations Method to Analyze Vascular Adaptation. Biomech. Model. Mechanobiol. 18, 29–44. doi:10.1007/s10237-018-1065-0 (2019)

[37] R. C. Cockrell, S. Christley, E. Chang and G. An. Towards anatomic scale agent-based modeling with a massively parallel spatially explicit general-purpose model of enteric tissue (SEGMEnT-HPC). PLoS ONE 10(3):1–14. doi:10.1371/journal.pone.0122192 (2015)

[38] H. N. Hayenga, B. C. Thorne, S. M. Peirce, J. D. Humphrey. Ensuring congruency in multiscale modeling: towards linking agent based and continuum biomechanical models of arterial adaptation. Ann Biomed Eng 39(11):2669–2682. doi:10.1007/s10439-011-0363-9 (2011)

[39]H. N. Hayenga, J. J. Hu, C. A. Meyer, E. Wilson, T. W. Hein, L. Kuo and J. D. Humphrey. Differential progressive remodeling of coronary and cerebral arteries and arterioles in an aortic coarctation model of hypertension. Front Physiol. doi:10.3389/fphys.2012.00420 (2012)

[40] M. J. North, N. T. Collier, J. Ozik, E. R. Tatara, C. M. Macal, M. Bragen, P. Sydelko. Complex adaptive systems modeling with repast simphony. Complex Adapt Syst Model 1(1):1–26. doi:10.1186/2194-3206-1-3 (2013)

[41] U. Wilensky and I. Evanston. NetLogo: center for connected learning and computer-based modeling. Northwestern University, Evanston. (1999)

[42] J. Macy and T. L. Horvath. Comparative Medicine: An Inclusive Crossover Discipline.
Yale J Biol Med. 2017 Sep 25;90(3):493-498. PMID: 28955187; PMCID: PMC5612191.

[43] H. A. Beilinson and C. A. Gianessi. Comparative Medicine.
Yale J Biol Med. 2017 Sep; 90(3): 347–350. Published online 2017 Sep 25. PMCID: PMC5612179

[44] E. C. Bryda. The Mighty Mouse: The Impact of Rodents on Advances in Biomedical Research.
Mo Med. 2013 May-Jun; 110(3): 207–211.
PMCID: PMC3987984 | NIHMSID: NIHMS570066 | PMID: 23829104

[45] R. A. Gibbs, et al. Genome sequence of the Brown Nor way rat yields insights into mammalian evolution. Nature. 2004; 428:493–521

[46] E. S. Lander, et al. Initial sequencing and analysis of the human genome. Nature. 2001; 409:860–921

[47] J. C. Venter, et al. The sequence of the human genome. Science. 2001; 291:1304–51

[48] R. H. Waterston RH, et al. Initial sequencing and comparative analysis of the mouse genome. Nature. 2002; 420:520–62

[49] A. W. Cowley Jr, M. Liang, R. J. Roman, A. S. Greene, H. J. Jacob. Consomic rat model systems for physiological genomics. Acta Physiol Scand. 2004; 181:585–92

[50] A. E. Kwitek-Black and H. J. Jacob. The use of designer rats in the genetic dissection of hypertension. Curr Hypertens Rep. 2001; 3:12

[51] R. Wernersson, M. H. Schierup, F. G. Jorgensen, J. Gorodkin , F. Panitz, H. H. Staerfeldt, et al. Pigs in sequence space: a 0.66X coverage pig genome survey based on shotgun sequencing. BMC Genomics. 2005; 6:70 (2005)

[52] E. M. Walters and R. S. Prather. Advancing Swine Models for Human Health and Diseases. Mo Med. 2013 May-Jun; 110(3): 212–215. PMCID: PMC6179855 | PMID: 23829105 (2013)

[53] J. Luan, L. Mao, Z. Zhu, W. Fu and T. Zhu. New indicators for systematic assessment of aortic morphology: a narrative review. J Thorac Dis. 2021 Jan; 13(1): 372–383. PMCID: PMC7867839 | PMID: 33569218. doi: 10.21037/jtd-20-2728 (2021)

[54] R. M. Lang, M. Bierig, R. B. Devereux, et al. Recommendations for chamber quantification: A report from the American Society of Echocardiography's guidelines and standards committee and the Chamber Quantification Writing Group, developed in conjunction with the European Association of Echocardiograph. J Am Soc Echocardiogr 2005; 18:1440-63. 10.1016/j.echo.2005.10.005 (2005)

[55] A. Wolak, H. Gransar, L. E. J. Thomson, et al. Aortic Size Assessment by Noncontrast Cardiac Computed Tomography: Normal Limits by Age, Gender, and Body Surface Area. JACC Cardiovasc Imaging 2008; 1:200-9. 10.1016/j.jcmg.2007.11.005

[56] P. Biaggi, F. Matthews, J. Braun, et al. Gender, Age, and Body Surface Area are the Major Determinants of Ascending Aorta Dimensions in Subjects With Apparently Normal Echocardiograms. J Am Soc Echocardiogr 2009;22:720-5. 10.1016/j.echo.2009.03.012 (2009)

[57] Average weight and growth chart for babies, toddlers, and kids | Babycenter. (2022) Available at: https://www.babycenter.com/baby/baby-development/average-weight-and-growth-chart-for-babies-toddlers-and-beyo_10357633

[58] Growth and Your 2- to 3-Year-Old | Nemours Kids Health. (2019). Available at: https://kidshealth.org/en/parents/growth-2-to 3.html#:~:text=During%20the%20third%20year%20of,learning%20in%20very%20physical%20ways

[59] High blood pressure in children | Mayo Clinic. (2021). Available at: https://www.mayoclinic.org/diseases-conditions/high-blood-pressure-in-children/symptoms-causes/syc-20373440

[60] M. Latorre, B. Spronck, J.D. Humphrey, Complementary roles of mechanotransduction and inflammation in vascular homeostasis. Proc. R. Soc. A 477: 20200622. https://doi.org/10.1098/rspa.2020.0622 (2021)

[61] M.S. Zimmerman, A.S.C. Smith, C.A. Sable, M.M. Echko, L.B. Wilner, H.E. Olsen, et al. Global, regional, and national burden of congenital heart disease, 1990–2017: a systematic analysis for the Global Burden of Disease Study 2017. Lancet Child Adolesc Health. 2020; 4:185–200. doi: 10.1016/S2352-4642(19)30402-X (2020)

[62] T. Aldersley, J. Lawrenson, M. Ngoepe, L. Swanson, A. Revell, B. Keavney, L. Zuhlke, et. al, PROTEA, A Southern African Multicenter Congenital Heart Disease Registry and Biorepository: Rationale, Design, and Initial Results. Front Pediatr. 2021; 9: 763060. doi: 10.3389/fped.2021.763060 (2021)

[63] N. Laing, S. Kraus, G. Shaboodien, N. Ntusi, An overview of thegenetic basis of cardiovascular disease. S Afr Med J. 2019; 109:364–70. doi: 10.7196/SAMJ. 2019.v109i6.14069 (2019)

[64] C. N. Rotimi, A. R. Bentley, A.P. Doumatey, G. Chen, D. Shriner, A. Adeyemo, The genomic landscape of African populations in health and disease. Hum Mol Genet. 2017; 26: R225–36. doi: 10.1093/hmg/ddx253 (2017)

[65] L. Swanson, M. Ngoepe, L. Zuhlke, The Development of a Patient-Specific, Open-Source Computational Fluid Dynamics Tool to Comprehensively and Innovatively Study Coarctation of the Aorta in a Limited Resource Clinical Context. University of Cape Town, Department of Mechanical Engineering. doi: https://open.uct.ac.za/server/api/core/bitstreams/dce6c651-5fce-4c78-837e-edf782838aa0/content (2019)

[66] C. P. Cardozo, Mechanotransduction: Overview. Encyclopedia of Bone Biology. 2020; 217 doi: https://doi.org/10.1016/B978-0-12-801238-3.62233-X (2020)

[67] M. A. Reidy, Growth factors and arterial smooth muscle cell proliferationa. Ann N Y Acad Sci 714(1):225–230. doi: 10.1111/j.1749-6632. 1994.tb12047.x [PubMed: 8017771] (1994)

[68] J. P. Stegemann, R. M. Nerem RM, Altered response of vascular smooth muscle cells to exogenous biochemical stimulation in two- and three-dimensional culture. Exp Cell Res 283(2):146–155. doi: 10.1016/S0014-4827(02)00041-1 [PubMed: 12581735] (2003)

[69] G. B. Chapman, W. Durante, J. D. Hellums, A. I. Schafer, Physiological cyclic stretch causes cell cycle arrest in cultured vascular smooth muscle cells. Am J Physiol Heart Circ Physiol 278(3):H748–54 [PubMed: 10710342] (2000)

[70] Z. Li, S. Moore, M. Z. Alavi, Mitogenic factors released from smooth muscle cells are responsible for neointimal cell proliferation after balloon catheter deendothelialization. Exp Mol Pathol 63(2):77–86. doi: 10.1006/exmp.1995.1032 [PubMed: 8941042] (1995)

[71] Y. H. Ma, S. Ling, H. E. Ives, Mechanical strain increases PDGF-B and PDGF β receptor expression in vascular smooth muscle cells. Biochem Biophys Res Commun 265(2):606–610. doi: 10.1006/bbrc.1999.1718 [PubMed: 10558917] (1999)

[72] A. J. Kanai, H. C. Strauss, G. A. Truskey, A. L. Crews, S. Grunfeld, T. Malinski, Shear stress induces ATP-independent transient nitric oxide release from vascular endothelial cells, measured directly with a porphyrinic microsensor. Circ Res 77(2):284–293. doi: 10.1161/01.RES.77.2.284 [PubMed: 7614715] (1995)

[73] H. J. Hsieh, N. Q. Li, J. A. Frangos, Shear stress increases endothelial platelet-derived growth factor mRNA levels. Am J Physiol 260(2 Pt 2):H642–6 [PubMed: 1996708] (1991)

[74] T. Ziegler, K. Bouzourene, V. J. Harrison, H. R. Brunner, D. Hayoz D, Influence of oscillatory and unidirectional flow environments on the expression of endothelin and nitric oxide synthase in cultured endothelial cells. Arterioscler Thromb Vasc Biol 18(5):686–692. doi: 10.1161/01.ATV.18.5.686 [PubMed: 9598825] (1998)

[75] Fiddler AI website. doi: https://www.fiddler.ai/model-accuracy-vs-model-performance/which-is-more-important-model-performance-or-model-accuracy#:~:text=Generally%20speaking%2C%20industry%20standards%20for,demand%2099%25%20accuracy%20and%20up. (2023)

[76] R. Hendricks, What is a good accuracy score in Machine Learning. doi: https://deepchecks.com/question/what-is-a-good-accuracy-score-in-machine-learning/#:~:text=Industry%20standards%20are%20between%2070,various%20businesses%20and%20sectors'%20needs.

[77] R. M. Sibly, J. H. Brown, Toward a physiological explanation of juvenile growth curves. Journal of Zoology. doi: 10.1111/jzo.12770 (2020)

[78] P. Henderson, R. Seaby, R. Somes, Growth II - a major upgrade to our 'Simply Growth' software. Fits and plots von Bertalanffy, Gompertz, Logistic and a wide range of other growth curves to length and/or weight at age data. Pisces Conservation Ltd. doi: http://www.pisces-conservation.com/pdf/growthiihelp.pdf (2006)

[79] D. E. Wachenheim, J. A. Patterson, M. R. Ladisch, Analysis of the logistic function model: derivation and applications specific to batch cultured microorganisms. Bioresource Technology 86(2): 157-164. doi: https://doi.org/10.1016/S0960-8524(02)00149-9 (2003)

[80] K. M. C. Tjorve, E. Tjorve, The use of Gompertz models in growth analyses, and new Gompertz-model approach: An addition to the Unified-Richards family. PLoS ONE 12(6):e0178691. doi: 10.1371/journal.pone.0178691 (2017)

[81] L. P. Hu, X. L. Bao, Q. Wang, The repetition principle in scientific research. National Library of Medicine: National center of biotechnology information 9(9):937-40.doi: 10.3736/jcim20110903 (2011)

[82] S. Slutz, K. L. Hess, Increasing the Ability of an Experiment to Measure an Effect. Science buddies website. doi:https://www.sciencebuddies.org/science-fair-projects/competitions/experimental-design-increasing-signal-to-noise

[83] J. D. Humphrey, K. R. Rajagopal, A constrained mixture model for arterial adaptations to a sustained step change in blood flow. Biomech Model Mechanobiol 2:109-126. doi: 10.1007/s10237-003-0033-4. (2003)

[84] J. M. Dolan, J. Kolega, H. Meng, High Wall Shear Stress and Spatial Gradients in Vascular Pathology: A Review. Ann Biomed Eng 41(7): 1411-1427. doi: 10.1007/s10439-012-0695-0 (2023)

[85] L. A. Taber, A Model for Aortic Growth Based on Fluid Shear and Fiber Stresses. *J Biomech Eng*. Jun 1998, 120(3): 348-354. doi: https://doi.org/10.1115/1.2798001 (1998)

[86] J. Rodriguez, J. M. Goicolea, F. Gabaldon, A volumetric model for growth of arterial walls with arbitrary geometry and loads. Journal of Biomechanics 40 (2007) 961–971. doi: https://doi.org/10.1016/j.jbiomech.2006.05.002 (2007)

[87] J. E. Wagenseil, A constrained mixture model for developing mouse aorta. Biomech Model Mechanobiol. 2011 Oct; 10(5): 671–687. doi: 10.1007/s10237-010-0265-z (2010)

[88] P. W. Alford, J. D. Humphrey, L. A. Taber, Growth and remodeling in a thick-walled artery model: effects of spatial variations in wall constituents. Biomech Model Mechanobiol;7(4):245–262. doi: https://doi.org/10.1007/s10237-007-0101-2 (2008)

[89] A. Valentin, L. Cardamone, S. Baek, J. D. Humphrey, Complementary vasoactivity and matrix remodelling in arterial adaptations to altered flow and pressure. J R Soc Interface; 6(32):293–306. doi: 92812083762PK762 (2008)

[90] A. Valentin, J. D. Humphrey, Modeling effects of axial extension on arterial growth and remodeling. Med Biol Eng Comput. 2009;47(9):979987. doi: 10.1007/s11517-009-0513-5 (2009)

[91] W. Wan, L. Hansen, R. L. Gleason Jr., A 3-d constrained mixture model for mechanically mediated vascular growth and remodeling. Biomech Model Mechanobiol; 9, 403–419. doi:https://doi.org/10.1007/s10237-009-0184-z (2009)

[92] R. L. Gleason, L. A. Taber, J. D. Humphrey, A 2-d model of flow-induced alterations in the geometry, structure and properties of carotid arteries. J Biomech Eng; 126:371–381. doi: https://doi.org/10.1159/000080699 (2004)

[93] C. S. Roy, The elastic properties of the arterial wall. Philos Trans R Soc Lond [Biol] 99: 1–31. (1880)

[94] M. Lefevre, R. B. Rucker, Aorta elastin turnover in normal and hypercholesterolemic Japanese quail. Biochim Biophys Acta. 1980 Jul 15;630(4):519-29. doi: 10.1016/0304-4165(80)90006-9. (1980)

Appendix 3.2

Slice ID	Slice 1 (before CoA)
Slice Geometry	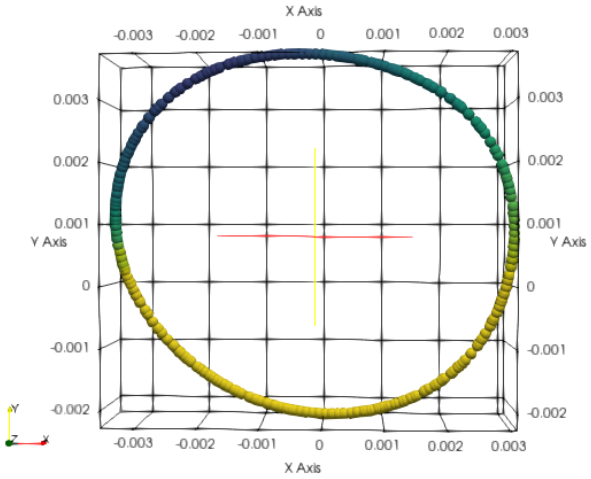
Point coordinate bounds	Bounds X Range: -0.00355583 to 0.00310306 (delta: 0.0066589) Y Range: -0.00227132 to 0.0037404 (delta: 0.00601173) Z Range: 0.00349362 to 0.00500822 (delta: 0.0015146)
Disc area (m^2)	3.26786e-05
Mechanical stress metrics	Showing DescriptiveStatistics4 (S Attribute: Row Data Precision: 6

	Maximum	Mean	Minimum	Variable
0	0.0046459	0.00301013	0.00125465	OverallWSS
1	0.00155206	-0.000143602	-0.00317739	PAWSS_average_0
2	0.00221101	0.000329975	-0.00112346	PAWSS_average_1
3	0.00353004	0.00203145	0.000897671	PAWSS_average_2
4	3.16825e-07	9.98923e-08	1.77536e-10	fluctuationWSSPrime2Mean_average_0
5	3.48804e-07	9.056e-08	2.35972e-09	fluctuationWSSPrime2Mean_average_1
6	3.44615e-07	1.54895e-07	4.8085e-08	fluctuationWSSPrime2Mean_average_2
7	0.00512744	0.00308322	0.00135785	instantPAWSSmag_average
8	12.9051	12.8808	12.8463	p_average

Slice ID	Slice 2 (At CoA)
Slice Geoemtry	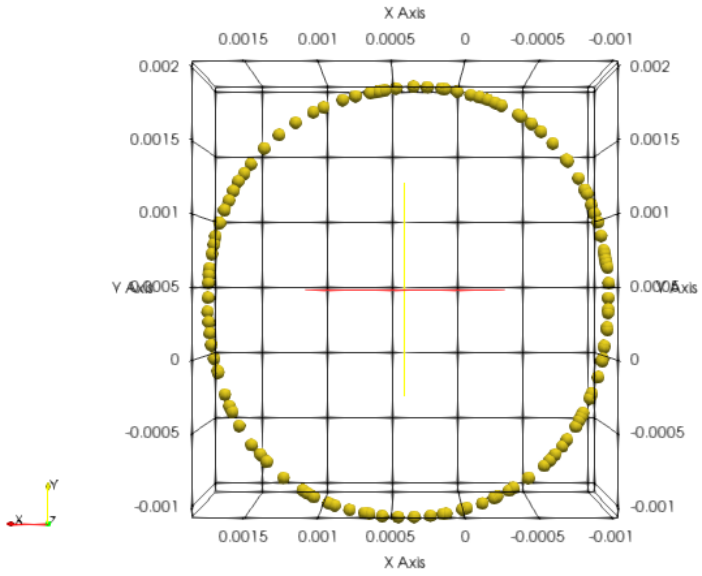
Point coordinate bounds	Bounds X Range: -0.00104299 to 0.00185968 (delta: 0.00290267) Y Range: -0.00106876 to 0.00203616 (delta: 0.00310492) Z Range: -0.000453266 to 0.000563027 (delta: 0.00101629)
Disc area (m^2)	7.58606e-06
Mechanical stress metrics	**Showing** DescriptiveStatistics5 (Statis **Attribute:** Row Data **Precision:** 6

	Maximum	Mean	Minimum	Variable
0	0.0722702	0.0552357	0.0376712	OverallWSS
1	0.011425	-0.0147478	-0.0337565	PAWSS_average_0
2	0.024918	-0.00205541	-0.017806	PAWSS_average_1
3	0.061829	0.0446138	0.0308965	PAWSS_average_2
4	8.37358e-06	3.82292e-06	3.34686e-07	fluctuationWSSPrime2Mean_average_0
5	8.57239e-06	3.2629e-06	4.10263e-07	fluctuationWSSPrime2Mean_average_1
6	3.29468e-05	1.69499e-05	7.21923e-06	fluctuationWSSPrime2Mean_average_2
7	0.06718	0.0525032	0.0374975	instantPAWSSmag_average
8	12.3445	12.1045	11.8546	p_average

Slice ID	Slice 3 (after CoA)
Slice Geometry	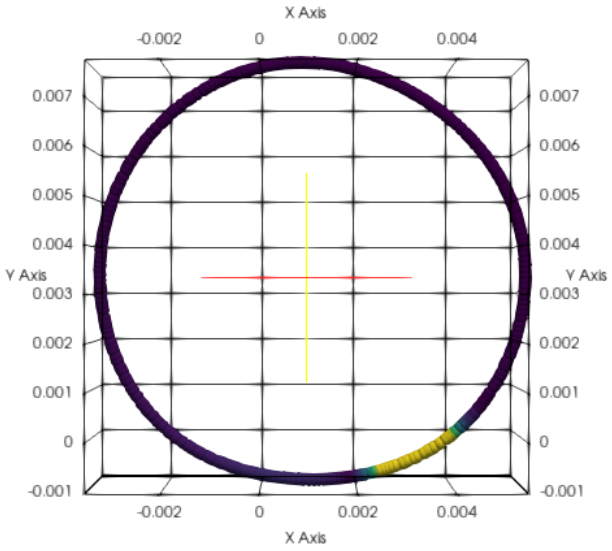
Point coordinate bounds	Bounds X Range: -0.00351827 to 0.00543839 (delta: 0.00895667) Y Range: -0.00103022 to 0.00774772 (delta: 0.00877794) Z Range: -0.00621272 to -0.00417526 (delta: 0.00203746)
Disc area (m^2)	6.37614e-05
Mechanical stress metrics	**Showing** DescriptiveStatistics6 (Statis **Attribute:** Row Data **Precision:** 6 10

	Maximum	Mean	Minimum	Variable
0	0.0121834	0.00223422	0.000481823	OverallWSS
1	0.00077198	-0.000227144	-0.00229166	PAWSS_average_0
2	0.00035634	-0.00010327	-0.00161916	PAWSS_average_1
3	0.00719054	0.00042876	-0.000586971	PAWSS_average_2
4	8.06099e-06	9.96648e-07	2.13153e-09	fluctuationWSSPrime2Mean_average_0
5	1.43705e-06	2.97861e-07	6.20389e-08	fluctuationWSSPrime2Mean_average_1
6	3.42392e-05	4.80196e-06	1.86102e-07	fluctuationWSSPrime2Mean_average_2
7	0.00882802	0.00138401	0.000331812	instantPAWSSmag_average
8	12.0526	12.0486	12.0301	p_average